EMBRY-RIDDLE
Aeronautical University
SCHOLARLY COMMONS

Theses - Daytona Beach | Dissertations and Theses

Summer 2010

Extension to Multiple Species of a Two-Equation Turbulence Model for High Speed Flows

Martin Horvath
Embry-Riddle Aeronautical University - Daytona Beach

Follow this and additional works at: https://commons.erau.edu/db-theses

Part of the Aerospace Engineering Commons

Scholarly Commons Citation

Horvath, Martin, "Extension to Multiple Species of a Two-Equation Turbulence Model for High Speed Flows" (2010). *Theses - Daytona Beach*. 87.
https://commons.erau.edu/db-theses/87

This thesis is brought to you for free and open access by Embry-Riddle Aeronautical University – Daytona Beach at ERAU Scholarly Commons. It has been accepted for inclusion in the Theses - Daytona Beach collection by an authorized administrator of ERAU Scholarly Commons. For more information, please contact commons@erau.edu.

EXTENSION TO MULTIPLE SPECIES OF A TWO-EQUATION TURBULENCE MODEL FOR HIGH SPEED FLOWS

by

Martin Horvath

A Thesis Submitted to the

Graduate Studies Office

in Partial Fulfillment of the Requirements for the Degree of

Master of Science in Aerospace Engineering

Embry-Riddle Aeronautical University

Daytona Beach, Florida

Summer 2010

UMI Number: EP31909

INFORMATION TO USERS

The quality of this reproduction is dependent upon the quality of the copy submitted. Broken or indistinct print, colored or poor quality illustrations and photographs, print bleed-through, substandard margins, and improper alignment can adversely affect reproduction.
In the unlikely event that the author did not send a complete manuscript and there are missing pages, these will be noted. Also, if unauthorized copyright material had to be removed, a note will indicate the deletion.

UMI®

UMI Microform EP31909
Copyright 2011 by ProQuest LLC
All rights reserved. This microform edition is protected against unauthorized copying under Title 17, United States Code.

ProQuest LLC
789 East Eisenhower Parkway
P.O. Box 1346
Ann Arbor, MI 48106-1346

EXTENSION TO MULTIPLE SPECIES

OF A TWO-EQUATION TURBULENCE MODEL

FOR HIGH SPEED FLOWS

by

Martin Horvath

This thesis was prepared under the direction of the candidate's thesis committee chairman, Dr. Eric Perrell, Department of Aerospace Engineering, and has been approved by the members of his thesis committee. It was submitted to the Aerospace Engineering Department and was accepted in partial fulfillment of the requirements for the degree of Master of Science in Aerospace Engineering.

THESIS COMMITTEE:

Dr. Eric Perrell, Chairman

Dr. William Engblom, Member

Dr. Vladimir Golubev, Member

Dr. Reda Mankbadi, Member

Department Chair, Aerospace Engineering — Date: 8/5/2010

Dr. James Cunningham, Associate Vice President for Academics — Date: 8/20/10

ACKNOWLEDGEMENTS

The author would like to take this opportunity to express sincere gratitude to the Thesis Chairman, Dr. Eric Perrell, for the encouragement to undertake this challenging task and the guidance to make it a success. Also, the contributions of the Thesis Committee Members, Drs. Engblom, Golubev, and Mankbadi, are greatly appreciated. A special thanks to Dr. David Wilcox for several helpful discussions relating to his research.

The author also wishes to convey heartfelt appreciation to his wife and parents for their undying support in his pursuit of higher education.

ABSTRACT

Author: Martin Horvath

Title: Extension to Multiple Species of a Two-Equation Turbulence Model for High Speed Flows

Institution: Embry-Riddle Aeronautical University

Degree: Master of Science in Aerospace Engineering

Year: 2010

The Wilcox (2006) k-ω turbulence model has been extended to multiple species and implemented in a CFD code for high speed flows using the Steger-Warming flux-vector splitting scheme. The model was chosen because compressibility corrections are not required, nor are viscous damping factors or wall functions to produce the law of the wall, and it has previously been validated for approximately one hundred test cases ranging from incompressible to hypersonic flow regimes. Initial validation cases using first-order accuracy have been performed, including a Mach 2.5 flow past a backward-facing step and a Mach 2.85 flow into a 24° compression corner. For the backward-facing step simulation, the surface pressure has a maximum error of 63% in the separation region, less than 5% error after the flow reattaches, and an RMS error of 17.2%, all of which are less than those of Wind-US and Cobalt. For the compression corner case, the surface pressure has a maximum error of 27% in the separation region, roughly 5% error downstream of separation, and an RMS error of 7.76%.

TABLE OF CONTENTS

ACKNOWLEDGEMENTS iii

ABSTRACT iv

LIST OF TABLES vii

LIST OF FIGURES viii

LIST OF SYMBOLS ix

Chapter

1. INTRODUCTION 1

1.1 Overview 1

1.2 Background 2

1.3 Approach 5

2. TURBULENCE MODELING 6

2.1 Reynolds Averaging 6

2.2 Favre Averaging 8

3. WILCOX k-ω TURBULENCE MODEL 11

3.1 Turbulence Model Equations 11

3.2 Improvements to Wilcox k-ω Model 15

4. IMPLEMENTATION OF k-ω MODEL IN CFD 16

4.1 CFD Code Description 16

4.2 Inviscid Fluxes 18

4.3 Viscous Fluxes 24

4.4 Source Terms 25

4.5 Boundary Conditions 26

5. VERIFICATION AND VALIDATION 28

5.1 Inviscid Verification Case 28

5.2 Mach 2.5 Flow past a Backward-Facing Step 30

5.3 Mach 2.85 Flow into a 24° Compression Corner 34

6. SUMMARY 41

6.1 Overview of Results 41

6.2 Future Recommendations 42

REFERENCES 43

APPENDIX 46

LIST OF TABLES

Table 1: Freestream Conditions - Backward-Facing Step 31

Table 2: Freestream Conditions – Compression Corner 36

LIST OF FIGURES

Figure 1: Scramjet Engine Operation 1

Figure 2: Percent Error - Inviscid Verification 29

Figure 3: Pressure Contours - Inviscid Verification 30

Figure 4: Computational Grid - Backward-Facing Step 31

Figure 5: Surface Pressure - Backward-Facing Step 32

Figure 6: Percent Error - Backward-Facing Step 33

Figure 7: Pressure Contours Backward-Facing Step 34

Figure 8: Computational Grid - Compression Corner 35

Figure 9: Surface Pressure – Compression Corner 37

Figure 10: Percent Error Compression Corner 38

Figure 11: Pressure Contours – Compression Corner 39

LIST OF SYMBOLS

English Symbols

a	Speed of sound
a_k	Augmented speed of sound
$\mathbf{A}, \mathbf{B}, \mathbf{C}$	Conservative flux Jacobian
$\widetilde{\mathbf{A}}, \widetilde{\mathbf{B}}, \widetilde{\mathbf{C}}$	Non-conservative flux Jacobian
c_p	Specific heat at constant pressure
C_{lim}	Stress-limiter strength
$\tilde{e}$	Favre-averaged specific internal energy
e_k	Specific kinetic energy
E	Specific total energy
f_β	Vortex-stretching function
$\mathbf{F}_\mathrm{I}, \mathbf{G}_\mathrm{I}, \mathbf{H}_\mathrm{I}$	Inviscid flux vectors in x, y, z directions
$\mathbf{F}_\mathrm{V}, \mathbf{G}_\mathrm{V}, \mathbf{H}_\mathrm{V}$	Viscous flux vectors in x, y, z directions
$\mathbf{F}'_\mathrm{I}, \mathbf{G}'_\mathrm{I}, \mathbf{H}'_\mathrm{I}$	Inviscid flux vectors in ξ, η, ζ directions
$\mathbf{F}'_\mathrm{V}, \mathbf{G}'_\mathrm{V}, \mathbf{H}'_\mathrm{V}$	Viscous flux vectors in ξ, η, ζ directions
$\mathbf{F}'^{+}, \mathbf{F}'^{-}$	Positive, negative flux vector
$\tilde{h}$	Favre-averaged specific enthalpy
h_f	Enthalpy of formation
k	Turbulence kinetic energy
k_s	Surface roughness height
$\mathbf{L}, \tilde{\mathbf{L}}$	Left eigenvectors of conservative, non-conservative flux Jacobian
P	Mean static pressure
Pr_T	Turbulent Prandtl number

q_L, q_T	Laminar, turbulent heat-flux vector
$\mathbf{Q}$	Conservative state vector
R	Gas constant
$\mathbf{R}, \widetilde{\mathbf{R}}$	Right eigenvectors of conservative, non-conservative flux Jacobian
$\mathbf{S}$	Source-term vector
S_{ij}	Mean strain-rate tensor
t	Time
$\tilde{T}$	Favre-averaged temperature
$u_i, \bar{u}_i$	Instantaneous, mean velocity
u_i', u_i''	Fluctuating, Favre fluctuating velocity
$\tilde{u}, \tilde{v}, \tilde{w}$	Favre-averaged velocity components in x, y, z directions
$\tilde{u}', \tilde{v}', \tilde{w}'$	Favre-averaged covariant velocity components in ξ, η, ζ directions
u_τ	Friction velocity
$\mathbf{V}$	Non-conservative state vector
x, y, z	Rectangular Cartesian coordinates (physical space)

Greek Symbols

γ	Specific heat ratio
δ_{ij}	Kronecker delta
κ	Thermal conductivity
$\mathbf{\Lambda}$	Eigenvalues of flux Jacobian
$\mathbf{\Lambda}^+, \mathbf{\Lambda}^-$	Positive, negative eigenvalues of flux Jacobian
μ	Molecular viscosity
μ_T	Eddy viscosity
ξ, η, ζ	Curvilinear coordinates (computational space)
ξ_i, η_i, ζ_i	Metrics
$\bar{\rho}$	Mean density of mixture

$\tilde{\tau}_{L_{ij}}, \tilde{\tau}_{T_{ij}}$	Laminar, Reynolds stress tensors (using Favre-averaged velocities)
χ_ω	Dimensionless vortex-stretching parameter
ω	Specific dissipation rate
Ω_{ij}	Mean-rotation tensor

Chapter 1

Introduction

1.1 Overview

The objective of this thesis project is to build the capability to do intensive Computational Fluid Dynamics (CFD) applications of hypersonic flows with non-equilibrium reaction modeling, and incorporating an appropriate means for modeling turbulence. One application of interest is a scramjet engine which has a complicated flow field including areas of compression, expansion, separation, recirculation, wall-bounded shear flows, and free jets. The operation of a scramjet engine is shown in Figure 1.

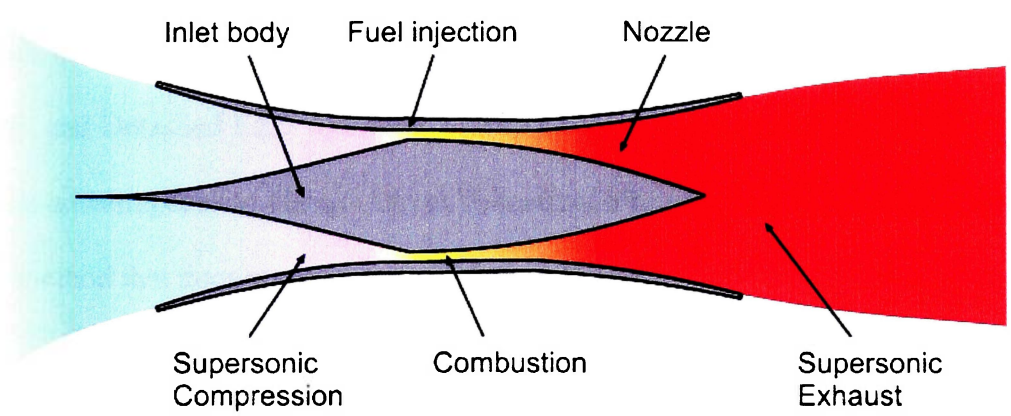

Figure 1: Scramjet Engine Operation

As can be seen from the geometry of the engine, a series of three-dimensional shock waves (oblique, reflected, and refracted) and expansion waves will be

created by the flow as it passes through the engine. Scramjet flows are characterized by turbulent shear layers, jets, wakes, and separated regions as a result of struts, injectors, steps, and structural seams, in addition to the high Reynolds number of the flow. Turbulent flow structures can effectively block parts of the flow, creating additional shock waves. Turbulent boundary layers change the displacement thickness, effectively altering the flow path geometry. Turbulence causes a loss of total pressure, increases heat transfer, and enhances mixing, hence combustion. Sufficiently accurate scramjet simulations cannot be achieved assuming laminar flow.

1.2 Background

There are a number of ways of dealing with turbulent flows, most of which involve modeling. The turbulence models that exist today vary in complexity and accuracy. The following is a survey of the different types of models including algebraic, one-equation, two-equation, Large Eddy Simulation (LES), and Detached Eddy Simulation (DES). Before looking at these models it will be advantageous to discuss Direct Numerical Simulation (DNS) which is the only method that does not require modeling turbulence.

DNS has the advantage of being the most accurate method because it solves the Navier-Stokes (N-S) equations directly using instantaneous flow-field information, with no modeling whatsoever. The disadvantage is that the computational limitation of present technology prevents solving the N-S

equations directly for non-trivial applications with turbulent flows. The limitation is the memory and CPU power required for the grid and time resolution needed to capture the turbulent eddies. For combustion applications, the problem is compounded by the addition of numerous species continuity equations. For more information on DNS consult the article by Moin and Mahesh [1].

Algebraic models, also known as zero-equation models, are the simplest type of turbulence model and are the easiest to implement. These models are incomplete in that the mixing length, which is used to determine the eddy viscosity, is dependent on the type of flow. Two popular models of this type are the Cebeci-Smith [2] and Baldwin-Lomax [3] models. The drawback of algebraic models is that they need to be tuned for specific flows using a database, and using the model for flows that vary from the database can produce unreliable results.

One-Equation models add a conservation equation for either the turbulence kinetic energy or the eddy viscosity. Early models that use the turbulence kinetic energy equation are incomplete, but later models that use an equation for the eddy viscosity are complete. The Baldwin-Barth [4] and Spalart-Allmaras [5] models both use an eddy viscosity equation and are thus complete. Although these complete models are an improvement over algebraic models because they do not require tuning for specific types of flows, they still have problems dealing with flows over a backward-facing step and shock-separated flows.

Two-Equation models provide an equation for the turbulence kinetic energy as well as its dissipation rate. Models of this type are complete and therefore do not require prior knowledge of the type of flow. Two widely used versions include the k-ω and k-ε models which have been developed by various researchers. The Launder-Sharma [6] model, also known as the Standard k-ε model, dates back to 1974. Perhaps the newest version of the k-ω model is that of Wilcox [7] which was revised in 2006. The k-ε model has shortcomings for wall-bounded flows in that it has problems dealing with adverse pressure gradients, and therefore separated flows. Also, it does not reproduce the law of the wall without using corrections. A third model is the Shear-Stress Transport (SST) model by Menter [8], which uses the k-ω model near walls and the k-ε model away from walls.

LES is a newer method for dealing with turbulence where only the small eddies are modeled, and the large eddies are computed directly. These smaller eddies are considered to be subgrid-scale (SGS), and the problem lies in developing an accurate SGS model. Although LES is less computationally expensive than DNS, it is still not useful for large-scale or complex turbulent flows until computer power increases. For more information on LES, consult the text by Sagaut and Germano [9].

DES is a blend of LES and the Reynolds-averaged Navier-Stokes (RANS) equations. LES is used for the largest eddies, and RANS with a turbulence model is used for boundary layers and thin shear layers. This method was introduced by

Spalart et al. [10]. The computation time for DES is much less than that for LES, and thus is the logical next step in the transition from RANS to LES.

1.3 Approach

A two-equation turbulence model will be added to an existing finite volume code for multi-species compressible flows, called HYP [11-13]. Steger-Warming flux-vector splitting [14] will be the upwind scheme used to capture shocks because it is a favorable method for hypersonic flows [15].

The Wilcox (2006) k-ω model [7] will be implemented for this project. This version of the k-ω model has had positive results for approximately 100 test cases, including but not limited to: attached boundary layers, free shear flows, backward-facing steps, and shock-separated flows. Other considerations that make the k-ω model more appealing than other turbulence models, such as the k-ε model, include not having to use viscous damping factors or wall functions to reproduce the law of the wall. Also, the k-ε model is not accurate for flows with adverse pressure gradients [16].

Chapter 2

Turbulence Modeling

This chapter presents some well-known results for the governing equations for turbulent flows. In some places the notation reflects the particular turbulence model used, which is described in the following chapter. For more detailed discussions and derivations, one may consult any of a number of excellent texts [17-19].

2.1 Reynolds Averaging

Turbulence is made up of swirling motions called eddies, the larger of which contain the most energy. They eventually decay into smaller eddies and finally dissipate into heat. Turbulent eddies are typically modeled as a fluctuating velocity. The instantaneous velocity (u_i) can then be expressed as the sum of the mean velocity ($\bar{u}_i$) and the fluctuating component (u_i').

$$u_i = \bar{u}_i + u_i' \tag{2.1}$$

For laminar flows, there are no fluctuations in the velocity. For steady flows, the mean velocity is constant for both laminar and turbulent flows.

Reynolds averaging, which is time averaging, is done as follows for the velocity or any flow variable.

$$\bar{u}_i = \lim_{T\to\infty} \frac{1}{T}\int_0^T u_i \, dt \tag{2.2}$$

The instantaneous values in the N-S equations are then replaced with the sum of Reynolds-averaged (mean) and fluctuating component. The N-S equations are then time-averaged resulting in averaged variables replacing their instantaneous counterparts, as well as extra terms involving the products of the fluctuating velocity components. These extra terms form the Reynolds-stress tensor defined below, which is the turbulent analog to the laminar shear-stress tensor.

$$\bar{\tau}_{T_{ij}} = -\rho\overline{u_i' u_j'} \tag{2.3}$$

For an incompressible flow, the conservation of momentum equation, in tensor notation, is then given by the following.

$$\rho\frac{\partial \bar{u}_i}{\partial t} + \rho\bar{u}_j\frac{\partial \bar{u}_i}{\partial x_j} = -\frac{\partial P}{\partial x_i} + \frac{\partial}{\partial x_j}\left(\bar{\tau}_{L_{ji}} + \bar{\tau}_{T_{ji}}\right) \tag{2.4}$$

The altered N-S equations are referred to as the Reynolds-averaged Navier-Stokes equations (RANS).

2.2 Favre Averaging

For compressible flows, the method of Reynolds averaging produces terms that do not parallel those found in the laminar equations. To compensate for this, Favre-averaging, which is mass-averaging, is used as shown below.

$$\tilde{u}_i = \frac{1}{\bar{\rho}} \lim_{T \to \infty} \frac{1}{T} \int_0^T \rho u_i \, dt \tag{2.5}$$

When using Favre-averaging, the notation for the mean and fluctuating components of the instantaneous flow-field variables is usually changed as follows:

$$u_i = \tilde{u}_i + u_i'' \tag{2.6}$$

A procedure similar to the Reynolds-averaging process is then followed, including variable substitution and time-averaging the N-S equations. The resulting form of the continuity equation is no different from the laminar case.

$$\frac{\partial \bar{\rho}}{\partial t} + \frac{\partial}{\partial x_i}(\bar{\rho}\tilde{u}_i) = 0 \tag{2.7}$$

The conservation of momentum equation differs from the laminar version with the addition of the Reynolds-stresses.

$$\frac{\partial}{\partial t}(\bar{\rho}\tilde{u}_i) + \frac{\partial}{\partial x_j}(\bar{\rho}\tilde{u}_j\tilde{u}_i) = -\frac{\partial P}{\partial x_i} + \frac{\partial}{\partial x_j}\left(\tilde{\tau}_{L_{ji}} + \tilde{\tau}_{T_{ji}}\right) \tag{2.8}$$

The modeled form of the conservation of energy equation introduces several new terms which need to be quantified. These terms include: turbulence kinetic energy (k) which is part of the total specific energy (E), turbulent heat-flux

vector (q_T), molecular diffusion and turbulent transport of turbulence kinetic energy which includes a closure coefficient (σ^*) and the specific dissipation rate (ω), and Reynolds-stress work.

$$\frac{\partial}{\partial t}(\bar{\rho}E) + \frac{\partial}{\partial x_j}\left[\tilde{u}_j(\bar{\rho}E + P)\right] = \frac{\partial}{\partial x_j}\left(-q_{L_j} - q_{T_j}\right) + \frac{\partial}{\partial x_j}\left[\left(\mu + \sigma^* \frac{\bar{\rho}k}{\omega}\right)\frac{\partial k}{\partial x_j}\right] + \frac{\partial}{\partial x_j}\left[\tilde{u}_i\left(\tilde{\tau}_{L_{ji}} + \tilde{\tau}_{T_{ji}}\right)\right] \tag{2.9}$$

The following equations describe the origins of the new terms. The turbulence kinetic energy, given from the correlation,

$$k = \frac{1}{2}\overline{u_i'' u_i''} \tag{2.10}$$

is identical in form to the specific kinetic energy with the exception that mean velocities are replaced with fluctuating velocities. The total specific energy, which now includes the turbulence kinetic energy, is given by the following equation.

$$E = \tilde{e} + \frac{1}{2}\tilde{u}_i\tilde{u}_i + k \tag{2.11}$$

The turbulent heat-flux vector is defined from a correlation of density, as well as velocity and enthalpy fluctuations.

$$q_{T_j} = \overline{\rho u_j'' h''} \tag{2.12}$$

The molecular diffusion and turbulent transport of turbulence kinetic energy arise from the following correlations respectively.

$$\left(\mu + \sigma^* \frac{\bar{\rho} k}{\omega}\right) \frac{\partial k}{\partial x_j} = \overline{\tau_{L_{ji}} u_i''} - \overline{\rho u_j'' \tfrac{1}{2} u_i'' u_i''} \tag{2.13}$$

The closure coefficient and the specific dissipation rate will be discussed further in Chapter 3. For completeness sake, the average pressure shown in the momentum and energy equations is calculated using the Reynolds-averaged density, the Favre-averaged temperature, and the gas constant.

$$P = \bar{\rho} R \tilde{T} \tag{2.14}$$

It is important to note that certain quantities have been defined in terms of fluctuating velocity components which are unknown. Determining correlations for these fluctuating components constitutes the "closure problem," which is solved largely by empirical methods. The particular approach is unique to the turbulence model employed.

In the next chapter we introduce a two-equation turbulence model which augments the N-S equations with conservation equations for turbulence kinetic energy and turbulence dissipation rate.

Chapter 3

Wilcox *k-ω* Turbulence Model

This chapter summarizes Wilcox's presentation [7] of his 2006 version of the *k-ω* model implemented here.

3.1 Turbulence Model Equations

The turbulence kinetic energy equation is derived by multiplying the instantaneous momentum equation by u_i'' and then time averaging. The following equation results after a considerable amount of algebra and making use of the continuity equation.

$$\begin{aligned}\frac{\partial}{\partial t}(\bar{\rho}k) + \frac{\partial}{\partial x_j}(\bar{\rho}\tilde{u}_j k) \\ &= \tilde{\tau}_{T_{ij}}\frac{\partial \tilde{u}_i}{\partial x_j} - \overline{\tau_{L_{ji}}\frac{\partial u_i''}{\partial x_j}} \\ &+ \frac{\partial}{\partial x_j}\left(\overline{\tau_{L_{ji}}u_i''} - \overline{\rho u_j''\tfrac{1}{2}u_i''u_i''} - \overline{p'u_j''}\right) - \overline{u_i''}\frac{\partial P}{\partial x_i} + \overline{p'\frac{\partial u_i''}{\partial x_i}}\end{aligned} \tag{3.1}$$

Analyzing this equation term by term, the left-hand side has the usual unsteady and convective terms. The first term on the right-hand side represents the rate of production of turbulence kinetic energy per unit volume, where the term "production" means a transfer of energy from the mean flow to turbulence. The

second term is dissipation: the rate of change of turbulence kinetic energy to heat, which is modeled by the following.

$$\overline{\tau_{L_{ji}} \frac{\partial u_i''}{\partial x_j}} = \beta^* \bar{\rho} k \omega \tag{3.2}$$

The closure coefficient (β^*) and the specific dissipation rate will be discussed later in this chapter. The third and fourth terms are the exact same correlations (eqn. 2.13) that appear in the conservation of energy equation, and therefore represent the molecular diffusion and turbulent transport of turbulence kinetic energy. The last three terms are pressure diffusion, pressure work, and pressure dilatation respectively. Pressure diffusion is modeled as part of the turbulent transport mentioned earlier due to the lack of experimental evidence to prove otherwise. Several models have been proposed for pressure work, but they have limited applicability [7]. Models for pressure dilatation are important for flows with a large turbulence production-to-dissipation ratio, such as cross-flows [20]. Thus, certain injector configurations may not be modeled well by this formulation. This is not the case for thin shear layers, such as boundary layers and mixing layers, which are the types of flows for which this model has been validated. The turbulence kinetic energy equation for this particular model is then given by the following, noting that the pressure work and pressure dilatation terms have been neglected.

$$\frac{\partial}{\partial t}(\bar{\rho} k) + \frac{\partial}{\partial x_j}(\bar{\rho} \tilde{u}_j k) = \tilde{\tau}_{T_{ij}} \frac{\partial \tilde{u}_i}{\partial x_j} - \beta^* \bar{\rho} k \omega + \frac{\partial}{\partial x_j}\left[\left(\mu + \sigma^* \frac{\bar{\rho} k}{\omega}\right) \frac{\partial k}{\partial x_j}\right] \tag{3.3}$$

Unlike the turbulence kinetic energy equation, the specific dissipation rate equation cannot be formally derived. Instead, it is proposed to have a similar form that includes unsteadiness, convection, production, dissipation, and diffusion. This particular model also employs cross diffusion which will be discussed later in this chapter. The specific dissipation rate equation is then given by the following, where the last term is the cross diffusion.

$$\begin{aligned}\frac{\partial}{\partial t}(\bar{\rho}\omega) + \frac{\partial}{\partial x_j}(\bar{\rho}\tilde{u}_j\omega) \\ = \alpha\frac{\omega}{k}\tilde{\tau}_{T_{ij}}\frac{\partial \tilde{u}_i}{\partial x_j} - \beta\bar{\rho}\omega^2 + \frac{\partial}{\partial x_j}\left[\left(\mu + \sigma\frac{\bar{\rho}k}{\omega}\right)\frac{\partial \omega}{\partial x_j}\right] \\ + \sigma_d\frac{\bar{\rho}}{\omega}\frac{\partial k}{\partial x_j}\frac{\partial \omega}{\partial x_j}\end{aligned} \tag{3.4}$$

As can be seen, many new closure coefficients have arisen in this equation.

At this point, the supplementary equations and closure coefficients for the turbulence model are presented. The laminar shear-stress and Reynolds-stress tensors are given by the following, noting that the Boussinesq approximation is used to calculate the Reynolds-stress.

$$\tilde{\tau}_{L_{ij}} = 2\mu\bar{S}_{ij}, \qquad \tilde{\tau}_{T_{ij}} = 2\mu_T\bar{S}_{ij} - \frac{2}{3}\bar{\rho}k\delta_{ij}, \qquad \bar{S}_{ij} = S_{ij} - \frac{1}{3}\frac{\partial \tilde{u}_k}{\partial x_k}\delta_{ij} \tag{3.5}$$

The mean strain-rate tensor (using Favre-averaged velocities) and the Kronecker delta are defined as:

$$S_{ij} = \frac{1}{2}\left(\frac{\partial \tilde{u}_i}{\partial x_j} + \frac{\partial \tilde{u}_j}{\partial x_i}\right) \qquad \delta_{ij} = \begin{cases}1, & i = j \\ 0, & i \neq j\end{cases} \tag{3.6}$$

The eddy viscosity, which is part of the Boussinesq approximation, uses the following equations to determine its value.

$$\mu_T = \frac{\bar{\rho}k}{\tilde{\omega}}, \qquad \tilde{\omega} = max\left\{\omega, \qquad C_{lim}\sqrt{\frac{2\bar{S}_{ij}\bar{S}_{ij}}{\beta^*}}\right\}, \qquad C_{lim} = \frac{7}{8} \tag{3.7}$$

Note that the eddy viscosity is limited by the value in the denominator. This is the stress-limiter that is discussed later in this chapter. The laminar and turbulent heat-flux vectors can be calculated from the following expressions.

$$q_{L_j} = -\kappa\frac{\partial\tilde{T}}{\partial x_j} \qquad q_{T_j} = -\frac{\mu_T c_p}{Pr_T}\frac{\partial\tilde{T}}{\partial x_j} \tag{3.8}$$

The closure coefficients required to complete the model are the following constants and expressions.

$$\alpha = \frac{13}{25}, \quad \beta^* = \frac{9}{100}, \quad \sigma = \frac{1}{2}, \quad \sigma^* = \frac{3}{5}, \quad Pr_T = \frac{8}{9} \tag{3.9}$$

$$\sigma_d = \begin{cases} 0, & \frac{\partial k}{\partial x_j}\frac{\partial \omega}{\partial x_j} \leq 0 \\ \sigma_{do}, & \frac{\partial k}{\partial x_j}\frac{\partial \omega}{\partial x_j} > 0 \end{cases}, \qquad \sigma_{do} = \frac{1}{8} \tag{3.10}$$

$$\beta = \beta_o f_\beta, \quad f_\beta = \frac{1+85\chi_\omega}{1+100\chi_\omega}, \quad \chi_\omega = \left|\frac{\Omega_{ij}\Omega_{jk}\hat{S}_{ki}}{(\beta^*\omega)^3}\right|, \quad \beta_o = 0.0708 \tag{3.11}$$

$$\Omega_{ij} = \frac{1}{2}\left(\frac{\partial\tilde{u}_i}{\partial x_j} - \frac{\partial\tilde{u}_j}{\partial x_i}\right) \qquad \hat{S}_{ki} = S_{ki} - \frac{1}{2}\frac{\partial\tilde{u}_m}{\partial x_m}\delta_{ki} \tag{3.12}$$

The equation for Ω_{ij} is the mean-rotation tensor, and S_{ki} is the mean strain-rate tensor as previously defined in Equation 3.6.

The RANS equations presented in Chapter 2, along with the turbulence model equations given here, are the complete set of equations required to deal with turbulent flows.

3.2 Improvements to Wilcox *k-ω* Model

The major improvements to the Wilcox (2006) *k-ω* model compared to the 1998 version include the addition of two components: a stress-limiter to the eddy viscosity, and cross diffusion to the specific dissipation rate equation. The stress-limiter reduces the eddy viscosity, which in turn limits the Reynolds-stresses when the dissipation of turbulence-energy is less than its production. This improves the accuracy for separated flows from the incompressible through to the hypersonic regions. The cross-diffusion term helps to diminish the sensitivity of the solution to the chosen freestream value for the specific dissipation rate. This in turn improves the accuracy for both free shear and wall-bounded flows. As a result of these improvements, compressibility corrections are no longer necessary resulting in the same closure coefficients being used for both the incompressible and compressible-flow versions of the model.

Chapter 4

Implementation of k-ω Model in CFD

4.1 CFD Code Description

The CFD code to which the turbulence model will be added is called HYP. The primary developer is Dr. Eric Perrell, and additional functionality has been added by Masters students over the years. HYP is a low-order, compressible-flow, CFD code written in Fortran 90. Some of the current capabilities include non-equilibrium chemically reacting flows and parallel processing. The turbulence model will be integrated with the code in a manner that makes use of both of these capabilities. At this time the code is not fully implicit, and for that reason the turbulence model will be coded explicitly. It is important to note that the inviscid fluxes will be capable of implicit calculation. For more information about HYP, please see the user's manual created by Francois Schmitt and Dr. Eric Perrell [21].

The conservation form of the RANS and turbulence model equations can be written in vector form for physical space (x, y, z) as follows:

$$\frac{\partial \mathbf{Q}}{\partial t} + \frac{\partial}{\partial x}(\mathbf{F}_\mathrm{I} - \mathbf{F}_\mathrm{V}) + \frac{\partial}{\partial y}(\mathbf{G}_\mathrm{I} - \mathbf{G}_\mathrm{V}) + \frac{\partial}{\partial z}(\mathbf{H}_\mathrm{I} - \mathbf{H}_\mathrm{V}) = \mathbf{S} \tag{4.1}$$

These equations can be transformed to computational space (ξ, η, ζ) resulting in:

$$\frac{\partial \mathbf{Q}}{\partial t} + \frac{\partial}{\partial \xi}(\mathbf{F}_{\mathrm{I}}' - \mathbf{F}_{\mathrm{V}}') + \frac{\partial}{\partial \eta}(\mathbf{G}_{\mathrm{I}}' - \mathbf{G}_{\mathrm{V}}') + \frac{\partial}{\partial \zeta}(\mathbf{H}_{\mathrm{I}}' - \mathbf{H}_{\mathrm{V}}') = \mathbf{S} \tag{4.2}$$

For this particular transformation method, the conservative state vector $(\mathbf{Q})$ remains the same for both the physical and computational domains.

$$\mathbf{Q} = \begin{bmatrix} \bar{\rho}_1 \\ \vdots \\ \bar{\rho}_{ns} \\ \bar{\rho}\tilde{u} \\ \bar{\rho}\tilde{v} \\ \bar{\rho}\tilde{w} \\ \bar{\rho}E \\ \bar{\rho}k \\ \bar{\rho}\omega \end{bmatrix} \tag{4.3}$$

Note that there is a continuity equation for each species to facilitate dealing with chemically reacting flows, and the mixture density $(\bar{\rho})$ is the sum of the species densities. Also, the internal energy must be calculated using standardized enthalpies for each species due to the chemical reactions. Making use of the definition of enthalpy and the ideal gas equation of state yields the following expression for the internal energy per unit volume.

$$\bar{\rho}\tilde{e} = P\frac{\sum_{s=1}^{ns} \bar{\rho}_s c_{p_s}}{\sum_{s=1}^{ns} \bar{\rho}_s R_s} + \sum_{s=1}^{ns} \bar{\rho}_s h_{f_s} - P \tag{4.4}$$

In this expression, the reference temperature for the enthalpy of formation (h_f) is absolute zero.

The difference between the physical and computational flux vectors, as well as the source terms, will be discussed in the sections that follow.

4.2 Inviscid Fluxes

The inviscid flux vectors in physical space are given by the following:

$$\mathbf{F}_{\mathrm{I}} = \begin{bmatrix} \bar{\rho}_1\tilde{u} \\ \vdots \\ \bar{\rho}_{ns}\tilde{u} \\ \bar{\rho}\tilde{u}^2 + P + \frac{2}{3}\bar{\rho}k \\ \bar{\rho}\tilde{u}\tilde{v} \\ \bar{\rho}\tilde{u}\tilde{w} \\ \tilde{u}\left(\bar{\rho}E + P + \frac{2}{3}\bar{\rho}k\right) \\ \bar{\rho}\tilde{u}k \\ \bar{\rho}\tilde{u}\omega \end{bmatrix} \quad \mathbf{G}_{\mathrm{I}} = \begin{bmatrix} \bar{\rho}_1\tilde{v} \\ \vdots \\ \bar{\rho}_{ns}\tilde{v} \\ \bar{\rho}\tilde{v}\tilde{u} \\ \bar{\rho}\tilde{v}^2 + P + \frac{2}{3}\bar{\rho}k \\ \bar{\rho}\tilde{v}\tilde{w} \\ \tilde{v}\left(\bar{\rho}E + P + \frac{2}{3}\bar{\rho}k\right) \\ \bar{\rho}\tilde{v}k \\ \bar{\rho}\tilde{v}\omega \end{bmatrix} \quad \mathbf{H}_{\mathrm{I}} = \begin{bmatrix} \bar{\rho}_1\tilde{w} \\ \vdots \\ \bar{\rho}_{ns}\tilde{w} \\ \bar{\rho}\tilde{w}\tilde{u} \\ \bar{\rho}\tilde{w}\tilde{v} \\ \bar{\rho}\tilde{w}^2 + P + \frac{2}{3}\bar{\rho}k \\ \tilde{w}\left(\bar{\rho}E + P + \frac{2}{3}\bar{\rho}k\right) \\ \bar{\rho}\tilde{w}k \\ \bar{\rho}\tilde{w}\omega \end{bmatrix} \tag{4.5}$$

The pressure like term $(\frac{2}{3}\bar{\rho}k)$ that appears in the momentum and energy equations is a component of the diagonal elements in the Reynolds-stress tensor, and it belongs with the inviscid fluxes because it is a first derivative in the system of equations. The flux vectors in computational space are found using the following transformations,

$$\mathbf{F}' = \xi_x\mathbf{F} + \xi_y\mathbf{G} + \xi_z\mathbf{H} \qquad \mathbf{G}' = \eta_x\mathbf{F} + \eta_y\mathbf{G} + \eta_z\mathbf{H} \qquad \mathbf{H}' = \zeta_x\mathbf{F} + \zeta_y\mathbf{G} + \zeta_z\mathbf{H} \tag{4.6}$$

where $\xi_x = \frac{\partial\xi}{\partial x}$, for example. These derivative terms in the transformations, which are determined by grid geometry, are known as metrics. In this particular transformation, the metrics are normalized as follows:

$$\xi_x^2 + \xi_y^2 + \xi_z^2 = 1 \qquad \eta_x^2 + \eta_y^2 + \eta_z^2 = 1 \qquad \zeta_x^2 + \zeta_y^2 + \zeta_z^2 = 1 \tag{4.7}$$

The metrics are also used to define the covariant velocities below.

$$\tilde{u}' = \xi_x\tilde{u} + \xi_y\tilde{v} + \xi_z\tilde{w} \qquad \tilde{v}' = \eta_x\tilde{u} + \eta_y\tilde{v} + \eta_z\tilde{w} \qquad \tilde{w}' = \zeta_x\tilde{u} + \zeta_y\tilde{v} + \zeta_z\tilde{w} \tag{4.8}$$

Using the transformations and the definitions of the covariant velocities, the inviscid flux vector in the ξ direction is given by:

$$\mathbf{F}_{\mathrm{I}}' = \begin{bmatrix} \bar{\rho}_1\tilde{u}' \\ \vdots \\ \bar{\rho}_{ns}\tilde{u}' \\ \bar{\rho}\tilde{u}\tilde{u}' + \xi_x\left(\frac{2}{3}\bar{\rho}k + P\right) \\ \bar{\rho}\tilde{v}\tilde{u}' + \xi_y\left(\frac{2}{3}\bar{\rho}k + P\right) \\ \bar{\rho}\tilde{w}\tilde{u}' + \xi_z\left(\frac{2}{3}\bar{\rho}k + P\right) \\ \left(\bar{\rho}E + P + \frac{2}{3}\bar{\rho}k\right)\tilde{u}' \\ \bar{\rho}k\tilde{u}' \\ \bar{\rho}\omega\tilde{u}' \end{bmatrix} \tag{4.9}$$

The inviscid flux vectors in the η and ζ directions are similar in form with the exception of the respective covariant velocities and metrics.

In this implementation, the inviscid fluxes are upwinded using Steger-Warming flux-vector splitting. Upwinding ensures that only information from the domain of dependence is used for the discretization of the fluxes. This is an important point as it allows the discretization to adapt to both subsonic and supersonic flows.

To start the process, the Euler equations in computational space can be rewritten as

$$\frac{\partial \mathbf{Q}}{\partial t} + \mathbf{A}\frac{\partial \mathbf{Q}}{\partial \xi} + \mathbf{B}\frac{\partial \mathbf{Q}}{\partial \eta} + \mathbf{C}\frac{\partial \mathbf{Q}}{\partial \zeta} = 0 \tag{4.10}$$

where the leading terms are the conservative flux Jacobians given by:

$$\mathbf{A} = \frac{\partial \mathbf{F}'}{\partial \mathbf{Q}} \qquad \mathbf{B} = \frac{\partial \mathbf{G}'}{\partial \mathbf{Q}} \qquad \mathbf{C} = \frac{\partial \mathbf{H}'}{\partial \mathbf{Q}} \tag{4.11}$$

Steger and Warming state that the flux vectors are homogeneous functions of degree one in $\mathbf{Q}$ if the equation of state is that of a perfect gas. This allows the flux vectors to be expressed as:

$$\mathbf{F}' = \mathbf{AQ} \qquad \mathbf{G}' = \mathbf{BQ} \qquad \mathbf{H}' = \mathbf{CQ} \tag{4.12}$$

A flux Jacobian can be decomposed into eigenvectors and eigenvalues as follows:

$$\mathbf{A} = \mathbf{R\Lambda L} \tag{4.13}$$

Here, the matrix of left eigenvectors ($\mathbf{L}$) is the inverse of the matrix of right eigenvectors ($\mathbf{R}$), and the eigenvalues ($\mathbf{\Lambda}$) are a diagonal matrix. The positive and negative fluxes can then be separated by using only the positive or negative eigenvalues in their respective calculations.

$$\mathbf{F}' = \mathbf{F}'^{+} + \mathbf{F}'^{-} = \mathbf{R\Lambda}^{+}\mathbf{LQ} + \mathbf{R\Lambda}^{-}\mathbf{LQ} \tag{4.14}$$

The method of determining the flux Jacobians, eigenvectors, and eigenvalues detailed by Hirsch [22] is used as a guideline for the present derivation. Finding the eigenvalues of the system is less complicated if the Euler equations are recast in non-conservative form using primitive variables

$$\frac{\partial \mathbf{V}}{\partial t} + \tilde{\mathbf{A}}\frac{\partial \mathbf{V}}{\partial \xi} + \tilde{\mathbf{B}}\frac{\partial \mathbf{V}}{\partial \eta} + \tilde{\mathbf{C}}\frac{\partial \mathbf{V}}{\partial \zeta} = 0 \tag{4.15}$$

where the leading terms are the non-conservative flux Jacobians given by:

$$\widetilde{\mathbf{A}} = \frac{\partial \mathbf{V}}{\partial \mathbf{Q}} \frac{\partial \mathbf{F}'}{\partial \mathbf{V}} \qquad \widetilde{\mathbf{B}} = \frac{\partial \mathbf{V}}{\partial \mathbf{Q}} \frac{\partial \mathbf{G}'}{\partial \mathbf{V}} \qquad \widetilde{\mathbf{C}} = \frac{\partial \mathbf{V}}{\partial \mathbf{Q}} \frac{\partial \mathbf{H}'}{\partial \mathbf{V}} \tag{4.16}$$

The non-conservative state vector ($\mathbf{V}$), which is required in the calculation of the Jacobian, has the following form:

$$\mathbf{V} = \begin{bmatrix} \bar{\rho}_1 \\ \vdots \\ \bar{\rho}_{ns} \\ \tilde{u} \\ \tilde{v} \\ \tilde{w} \\ P \\ k \\ \omega \end{bmatrix} \tag{4.17}$$

The first calculation for this derivation is a transformation matrix that is required to switch between conservative and non-conservative forms.

$$\frac{\partial \mathbf{Q}}{\partial \mathbf{V}} = \begin{bmatrix} 1 & 0 & 0 & 0 & 0 & 0 & 0 & 0 \\ 0 & 1 & 0 & 0 & 0 & 0 & 0 & 0 \\ \tilde{u} & \tilde{u} & \rho & 0 & 0 & 0 & 0 & 0 \\ \tilde{v} & \tilde{v} & 0 & \bar{\rho} & 0 & 0 & 0 & 0 \\ \tilde{w} & \tilde{w} & 0 & 0 & \bar{\rho} & 0 & 0 & 0 \\ h_{f_1} + \tilde{h}_1 - \frac{\gamma R_1 T}{\gamma - 1} + e_k + k & h_{f_{ns}} + \tilde{h}_{ns} - \frac{\gamma R_{ns} T}{\gamma - 1} + e_k + k & \bar{\rho}\tilde{u} & \rho\tilde{v} & \bar{\rho}\tilde{w} & \frac{1}{\gamma - 1} & \rho & 0 \\ k & k & 0 & 0 & 0 & 0 & \bar{\rho} & 0 \\ \omega & \omega & 0 & 0 & 0 & 0 & 0 & \rho \end{bmatrix} \tag{4.18}$$

To simplify the above result, the term e_k is used to represent the specific kinetic energy. The inverse of this transformation is also required, and is provided in the appendix due to its size. The non-conservative flux Jacobian ($\widetilde{\mathbf{A}}$) is then found using Equation 4.16 ($\frac{\partial \mathbf{F}'}{\partial \mathbf{V}}$ is given in the appendix).

$$\widetilde{\mathbf{A}} = \begin{bmatrix} \tilde{u}' & 0 & \xi_x\bar{\rho}_1 & \xi_y\bar{\rho}_1 & \xi_z\bar{\rho}_1 & 0 & 0 & 0 \\ 0 & \tilde{u}' & \xi_x\bar{\rho}_{ns} & \xi_y\bar{\rho}_{ns} & \xi_z\bar{\rho}_{ns} & 0 & 0 & 0 \\ \xi_x\frac{2k}{3\bar{\rho}} & \xi_x\frac{2k}{3\bar{\rho}} & \tilde{u}' & 0 & 0 & \xi_x\frac{1}{\bar{\rho}} & \xi_x\frac{2}{3} & 0 \\ \xi_y\frac{2k}{3\bar{\rho}} & \xi_y\frac{2k}{3\bar{\rho}} & 0 & \tilde{u}' & 0 & \xi_y\frac{1}{\bar{\rho}} & \xi_y\frac{2}{3} & 0 \\ \xi_z\frac{2k}{3\bar{\rho}} & \xi_z\frac{2k}{3\bar{\rho}} & 0 & 0 & \tilde{u}' & \xi_z\frac{1}{\bar{\rho}} & \xi_z\frac{2}{3} & 0 \\ 0 & 0 & \xi_x\bar{\rho}\left(a_k^2 - \frac{2}{3}k\right) & \xi_y\bar{\rho}\left(a_k^2 - \frac{2}{3}k\right) & \xi_z\bar{\rho}\left(a_k^2 - \frac{2}{3}k\right) & \tilde{u}' & 0 & 0 \\ 0 & 0 & 0 & 0 & 0 & 0 & \tilde{u}' & 0 \\ 0 & 0 & 0 & 0 & 0 & 0 & 0 & \tilde{u}' \end{bmatrix} \tag{4.19}$$

The remaining two flux Jacobians are similar in form with the exception of the respective covariant velocities and metrics. The speed of sound term in the Jacobian is defined as,

$$a_k = \sqrt{a^2 + \frac{2}{3}k\gamma} \tag{4.20}$$

where "a" is the speed of sound in the absence of turbulence ($a = \sqrt{\gamma RT}$). This term also appears in the eigenvalues of the Jacobian as shown below.

$$\mathbf{\Lambda} = \begin{bmatrix} \tilde{u}' & 0 & 0 & 0 & 0 & 0 & 0 & 0 & 0 \\ 0 & \ddots & 0 & 0 & 0 & 0 & 0 & 0 & 0 \\ 0 & 0 & \tilde{u}' & 0 & 0 & 0 & 0 & 0 & 0 \\ 0 & 0 & 0 & \tilde{u}' & 0 & 0 & 0 & 0 & 0 \\ 0 & 0 & 0 & 0 & \tilde{u}' & 0 & 0 & 0 & 0 \\ 0 & 0 & 0 & 0 & 0 & \tilde{u}' & 0 & 0 & 0 \\ 0 & 0 & 0 & 0 & 0 & 0 & \tilde{u}' & 0 & 0 \\ 0 & 0 & 0 & 0 & 0 & 0 & 0 & \tilde{u}' + a_k & 0 \\ 0 & 0 & 0 & 0 & 0 & 0 & 0 & 0 & \tilde{u}' - a_k \end{bmatrix} \tag{4.21}$$

Due to the inclusion of the $\frac{2}{3}\bar{\rho}k$ term in the inviscid fluxes, the speed of sound is augmented by the turbulence kinetic energy as previously found by Siikonen [23].

The non-conservative right and left eigenvectors for this system, $\tilde{\mathbf{R}}$ and $\tilde{\mathbf{L}}$, are presented in the appendix. The conservative forms of the eigenvectors are obtained by using the following transformations.

$$\mathbf{R} = \frac{\partial \mathbf{Q}}{\partial \mathbf{V}} \tilde{\mathbf{R}} \qquad \mathbf{L} = \tilde{\mathbf{L}} \frac{\partial \mathbf{V}}{\partial \mathbf{Q}} \tag{4.22}$$

Inspection of the left eigenvectors (in appendix) reveals a potential problem: the presence of metrics in the denominator can be destabilizing if sufficiently small. It can be shown that three variations of these eigenvectors exist, each with a different metric in the denominator. Therefore, all that is required to alleviate this problem is to compare the magnitudes of the metrics and choose the appropriate eigensystem such that the largest is in the denominator.

The explicit upwind scheme used for the inviscid fluxes is first-order accurate which may be insufficient, as will be seen in the upcoming chapter dealing with validation.

4.3 Viscous Fluxes

The viscous flux vectors in physical space are given by the following:

$$\mathbf{F}_{\mathrm{V}} = \begin{bmatrix} 0 \\ \vdots \\ 0 \\ 2\bar{S}_{xx}(\mu+\mu_T) \\ 2S_{xy}(\mu+\mu_T) \\ 2S_{xz}(\mu+\mu_T) \\ \left(\kappa + \frac{\mu_T c_p}{Pr_T}\right)\frac{\partial \tilde{T}}{\partial x} + \left(\mu + \sigma^* \frac{\bar{\rho}k}{\omega}\right)\frac{\partial k}{\partial x} + 2(\mu+\mu_T)\left(\tilde{u}\bar{S}_{xx} + \tilde{v}S_{xy} + \tilde{w}S_{xz}\right) \\ \left(\mu + \sigma^* \frac{\bar{\rho}k}{\omega}\right)\frac{\partial k}{\partial x} \\ \left(\mu + \sigma \frac{\bar{\rho}k}{\omega}\right)\frac{\partial \omega}{\partial x} \end{bmatrix} \tag{4.23}$$

$$\mathbf{G}_{\mathrm{V}} = \begin{bmatrix} 0 \\ \vdots \\ 0 \\ 2S_{yx}(\mu+\mu_T) \\ 2\bar{S}_{yy}(\mu+\mu_T) \\ 2S_{yz}(\mu+\mu_T) \\ \left(\kappa + \frac{\mu_T c_p}{Pr_T}\right)\frac{\partial \tilde{T}}{\partial y} + \left(\mu + \sigma^* \frac{\bar{\rho}k}{\omega}\right)\frac{\partial k}{\partial y} + 2(\mu+\mu_T)\left(\tilde{u}S_{yx} + \tilde{v}\bar{S}_{yy} + \tilde{w}S_{yz}\right) \\ \left(\mu + \sigma^* \frac{\bar{\rho}k}{\omega}\right)\frac{\partial k}{\partial y} \\ \left(\mu + \sigma \frac{\bar{\rho}k}{\omega}\right)\frac{\partial \omega}{\partial y} \end{bmatrix} \tag{4.24}$$

$$\mathbf{H}_{\mathrm{V}} = \begin{bmatrix} 0 \\ \vdots \\ 0 \\ 2S_{zx}(\mu+\mu_T) \\ 2S_{zy}(\mu+\mu_T) \\ 2\bar{S}_{zz}(\mu+\mu_T) \\ \left(\kappa + \frac{\mu_T c_p}{Pr_T}\right)\frac{\partial \tilde{T}}{\partial z} + \left(\mu + \sigma^* \frac{\bar{\rho}k}{\omega}\right)\frac{\partial k}{\partial z} + 2(\mu+\mu_T)\left(\tilde{u}S_{zx} + \tilde{v}S_{zy} + \tilde{w}\bar{S}_{zz}\right) \\ \left(\mu + \sigma^* \frac{\bar{\rho}k}{\omega}\right)\frac{\partial k}{\partial z} \\ \left(\mu + \sigma \frac{\bar{\rho}k}{\omega}\right)\frac{\partial \omega}{\partial z} \end{bmatrix} \tag{4.25}$$

The viscous flux vectors in computational space are found using the previously defined transformations. The viscous flux vector in the ξ direction is then given by:

$$\mathbf{F}_V' = \begin{bmatrix} 0 \\ \vdots \\ 0 \\ 2(\mu+\mu_T)(\xi_x\bar{S}_{xx}+\xi_y S_{yx}+\xi_z S_{zx}) \\ 2(\mu+\mu_T)(\xi_x S_{xy}+\xi_y\bar{S}_{yy}+\xi_z S_{zy}) \\ 2(\mu+\mu_T)(\xi_x S_{xz}+\xi_y S_{yz}+\xi_z\bar{S}_{zz}) \\ \left(\kappa+\frac{\mu_T c_p}{Pr_T}\right)\frac{\partial\xi}{\partial x_\iota}\frac{\partial\tilde{T}}{\partial x_\iota}+\left(\mu+\sigma^*\frac{\bar{\rho}k}{\omega}\right)\frac{\partial\xi}{\partial x_\iota}\frac{\partial k}{\partial x_\iota}+2(\mu+\mu_T)\frac{\partial\xi}{\partial x_\iota}\tilde{u}_j\bar{S}_{\iota j} \\ \left(\mu+\sigma^*\frac{\bar{\rho}k}{\omega}\right)\left(\xi_x\frac{\partial k}{\partial x}+\xi_y\frac{\partial k}{\partial y}+\xi_z\frac{\partial k}{\partial z}\right) \\ \left(\mu+\sigma\frac{\bar{\rho}k}{\omega}\right)\left(\xi_x\frac{\partial\omega}{\partial x}+\xi_y\frac{\partial\omega}{\partial y}+\xi_z\frac{\partial\omega}{\partial z}\right) \end{bmatrix} \tag{4.26}$$

The viscous flux vectors in the η and ζ directions are similar in form with the exception of the respective metrics. For the discretization of the derivative terms, a second-order accurate scheme is used.

4.4 Source Terms

The source terms for the turbulence model are given by the following:

$$\mathbf{S} = \begin{bmatrix} 0 \\ \vdots \\ \vdots \\ \vdots \\ \vdots \\ \vdots \\ 0 \\ \tilde{\tau}_{T_{\iota j}}\frac{\partial\tilde{u}_\iota}{\partial x_j}-\beta^*\bar{\rho}k\omega \\ \alpha\frac{\omega}{k}\tilde{\tau}_{T_{\iota j}}\frac{\partial\tilde{u}_\iota}{\partial x_j}-\beta\bar{\rho}\omega^2+\sigma_d\frac{\bar{\rho}}{\omega}\frac{\partial k}{\partial x_j}\frac{\partial\omega}{\partial x_j} \end{bmatrix} \tag{4.27}$$

All that is required for calculation in computational space is to apply the chain rule to the derivative terms. Similar to the viscous fluxes, the discretization is second-order accurate.

4.5 Boundary Conditions

Two boundary conditions of interest for the turbulence kinetic energy and specific dissipation rate are solid walls and the freestream. The treatment of the freestream will be addressed first.

Inspection of the turbulence model equations reveals that the turbulence kinetic energy and specific dissipation rate must be non-zero everywhere in the flow because they both appear in the denominator. The freestream values must then be determined.

To estimate the freestream turbulence kinetic energy it is helpful to use a quantity called the turbulence intensity which relates the turbulence kinetic energy to the freestream velocity. The ranges of turbulence intensity for different flow conditions are available from reputable online sources, commercial flow-solver user guides, and scholarly papers, allowing the freestream turbulence kinetic energy to then be estimated.

Wilcox [7] shows that the solution to free shear flows is sensitive to the value of the specific dissipation rate in the freestream, therefore it must be chosen

carefully. Although the cross diffusion term in the specific dissipation rate equation helps to reduce the sensitivity, it is wise to choose a freestream value that is less than 1% of the maximum to virtually eliminate the problem. This may require altering the freestream value as the simulation progresses.

The solid-wall boundary condition for the turbulence kinetic energy is simply zero due to the no-slip/no-penetration conditions. The specific dissipation rate is numerically problematic in that it is singular for a perfectly-smooth wall. As detailed by Wilcox [7], a "slightly-rough-surface boundary condition" can be used as an accurate alternative.

$$\omega = \frac{40000\mu}{\bar{\rho} k_s^2} \tag{4.28}$$

For a "hydraulically-smooth surface", the average height of sand-grain roughness (k_s) must be sufficiently small to satisfy the following:

$$\frac{\bar{\rho} u_\tau k_s}{\mu} < 5 \tag{4.29}$$

where u_τ is the friction velocity.

This concludes the discussion of the implementation of the turbulence model. Other texts consulted include those by Anderson [24] and Tannehill [25].

Chapter 5

Verification and Validation

To build confidence in the solutions obtained from CFD simulations, the code must first be verified to produce known analytical results and validated against experimental data. The following test cases constitute the start of this process.

5.1 Inviscid Verification Case

Using only the inviscid fluxes, a verification case can be run to check two items: the analytical results for an inviscid, compressible flow are obtained, and both the turbulence kinetic energy and specific dissipation rate are conserved in space. For this case, a supersonic flow into a compression corner, comprised of a single species (N_2), is used to create an oblique shock wave. Starting from the first grid point downstream of the shock, the percent error for the pressure, temperature, and velocity at the wall are plotted in Figure 2.

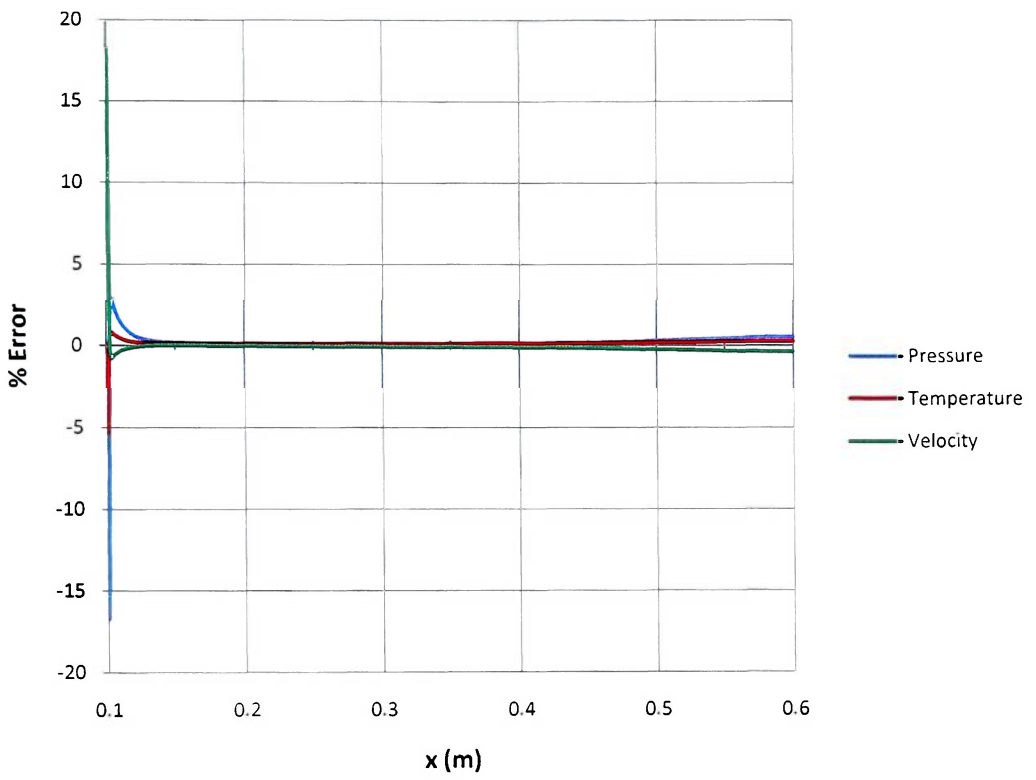

Figure 2: Percent Error - Inviscid Verification

The resolution of the shock wave is smeared across three cells which is why the error is large in that region. Once resolved, the error is less than 1% of the analytical results. The smeared shock wave is shown by the pressure contours in Figure 3.

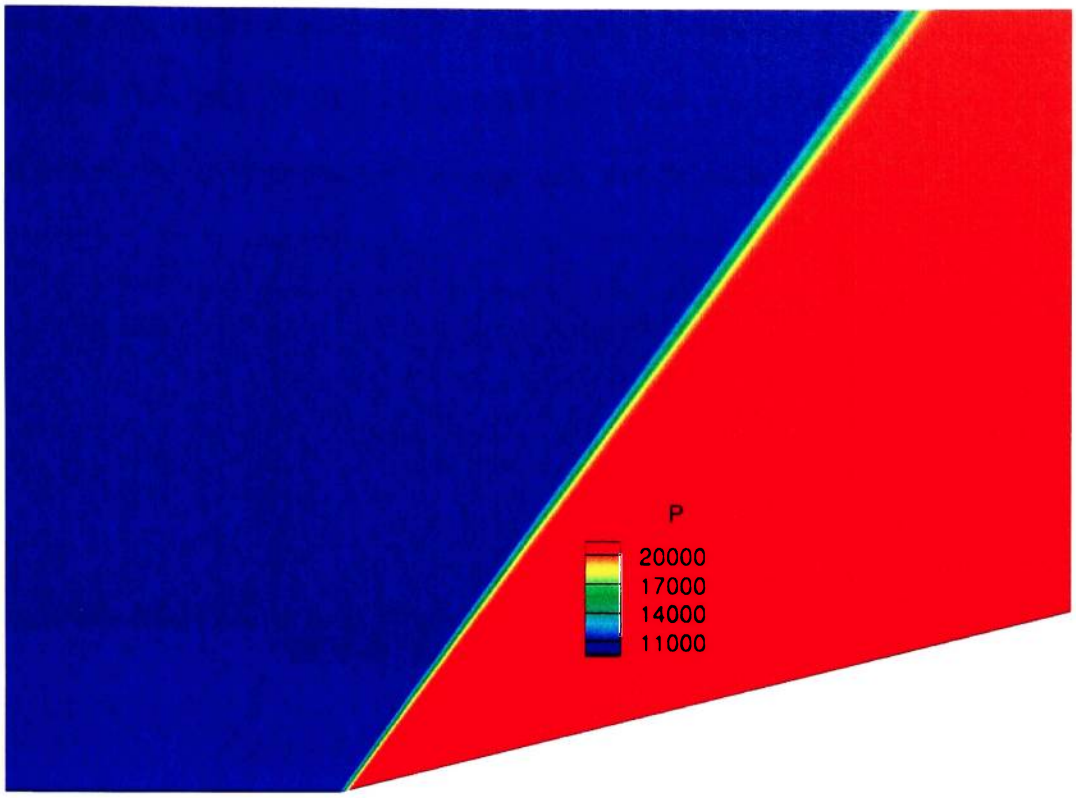

Figure 3: Pressure Contours - Inviscid Verification

Running the simulation using single precision will produce values for k and ω that are not precisely constant for the entire flow-field. Switching to double precision alleviates this problem, signifying that it is only round-off error.

This is the only quantified verification that has been performed, and an obvious test case for the future is to verify that the law of the wall is obeyed for a turbulent boundary layer.

5.2 Mach 2.5 Flow past a Backward-Facing Step

The experimental data of Smith [26], for a step-height of 0.443 inches, is used here for validation. The Wind-US code also uses this data for validation,

and the case can be found in the NPARC Alliance Verification and Validation Archive. The grid from that case, shown in Figure 4, is used here, and it consists of two blocks; one upstream of the step (red), and the other downstream (green).

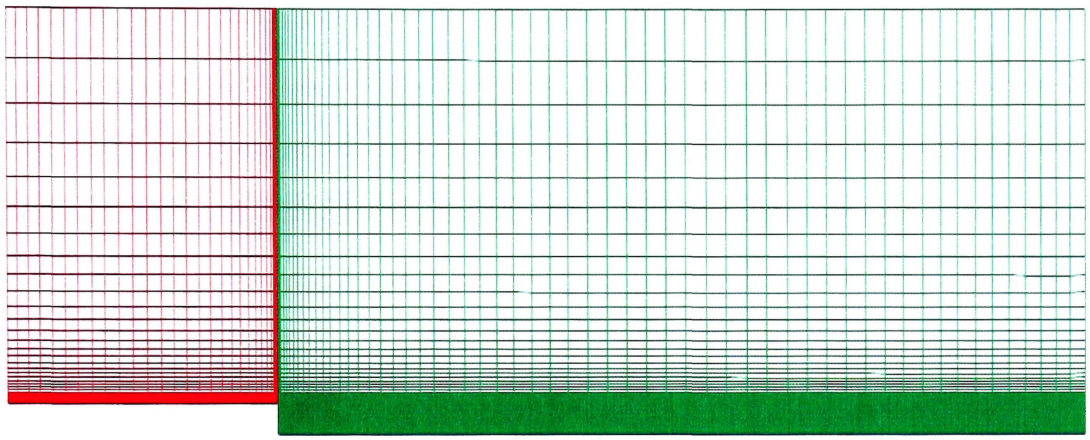

Figure 4: Computational Grid - Backward-Facing Step

To ensure adequate grid resolution in the boundary layer, the y^+ value of the first grid point from the walls is approximately one.

To simulate air, a two-species mixture composed of 79% N_2 and 21% O_2 is used. The freestream conditions for the simulation are given in Table 1, where the values in brackets come directly from the experiment.

Freestream Conditions	
T_∞ = 153 K	(T_o = 620 °R)
p_∞ = 13316 Pa	(p_o = 33 psi)
u_∞ = 620 m/s	(M_∞ = 2.5)
$k_\infty = 1E\text{-}8 * u_\infty^2 = 0.00384\ m^2/s^2$	
$\omega_\infty = 3900\ s^{-1}$	

Table 1: Freestream Conditions - Backward-Facing Step

The turbulence intensity (1E-8) and freestream specific dissipation rate are typical values used by Wilcox [27] in the companion software included with his book. A

surface-roughness height of 3.048 μm is used for the wall boundary-condition of the specific dissipation rate, also from Wilcox.

The results for the surface pressure are shown in Figure 5 where the step location corresponds to x = 0. They are compared to those of Wind-US using the HLLC scheme and the Menter SST turbulence model with compressibility corrections, and Cobalt with the Wilcox (1998) k-ω model.

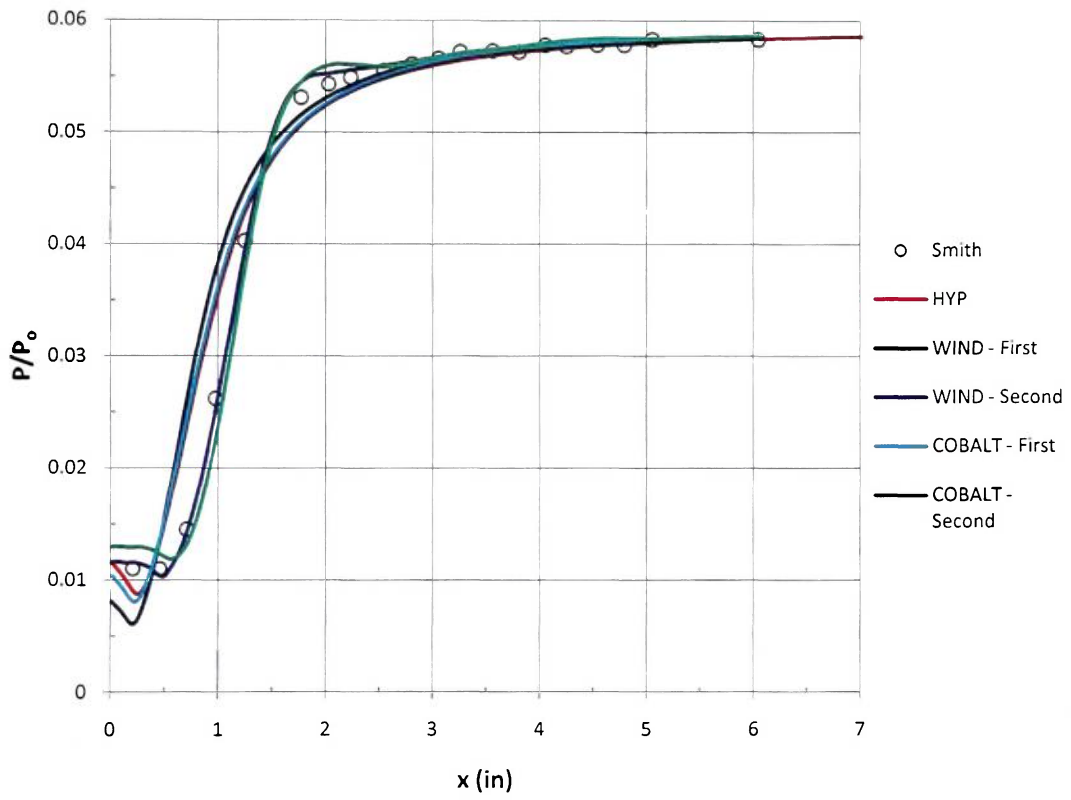

Figure 5: Surface Pressure - Backward-Facing Step

As expected, the second-order results are much better, with the Wind-US solver being the closest. A percent-error comparison of the first-order solutions is shown in Figure 6.

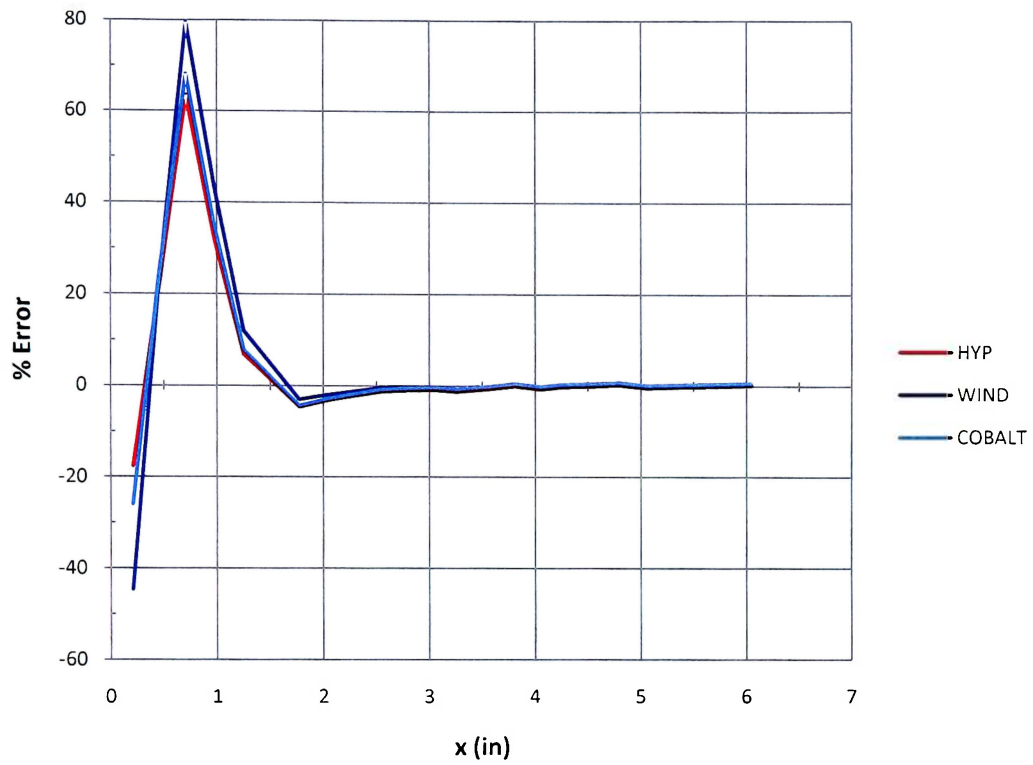

Figure 6: Percent Error - Backward-Facing Step

It can be seen that HYP, with the Wilcox (2006) k-ω model, performs better from the step up to x = 1.5, Wind-US has an advantage for a small region centered at x = 2, and all perform equally well after that. It should be noted that the error is significantly greater than 5% for all of the solvers for the first 1.5 inches behind the step. The RMS error for HYP, Wind-US, and Cobalt is 17.2, 23.3, and 19.0 percent respectively.

The pressure contours in Figure 7 show expansion waves originating at the corner of the step, and an oblique shock where the flow reattaches downstream.

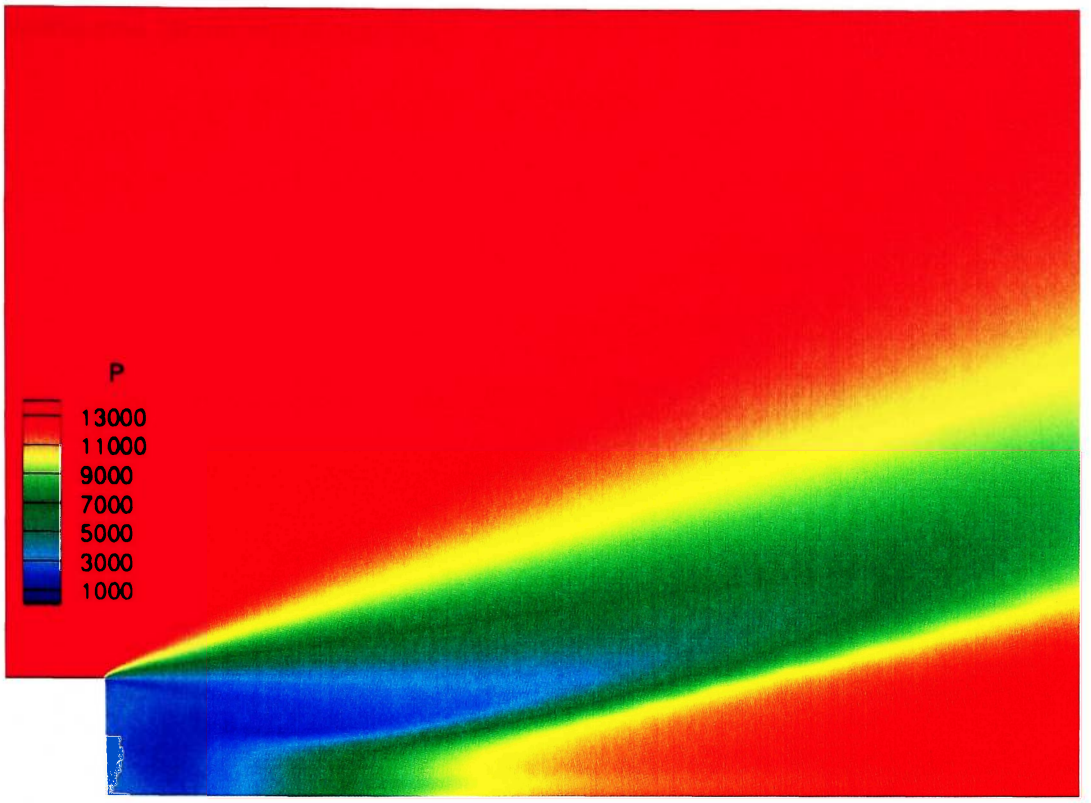

Figure 7: Pressure Contours - Backward-Facing Step

From this validation case it can be seen that although the first-order results are comparable to those of other flow solvers, a second-order upwind scheme should improve the accuracy of the solution considerably.

5.3 Mach 2.85 Flow into a 24° Compression Corner

For a second validation case, the experimental data of Settles, Vas, and Bogdonoff [28] is used. Wilcox [7] also uses this data for validation, and the grid from that case is used here. The grid is shown in Figure 8, noting that only every

fourth grid line is visible for clarity.

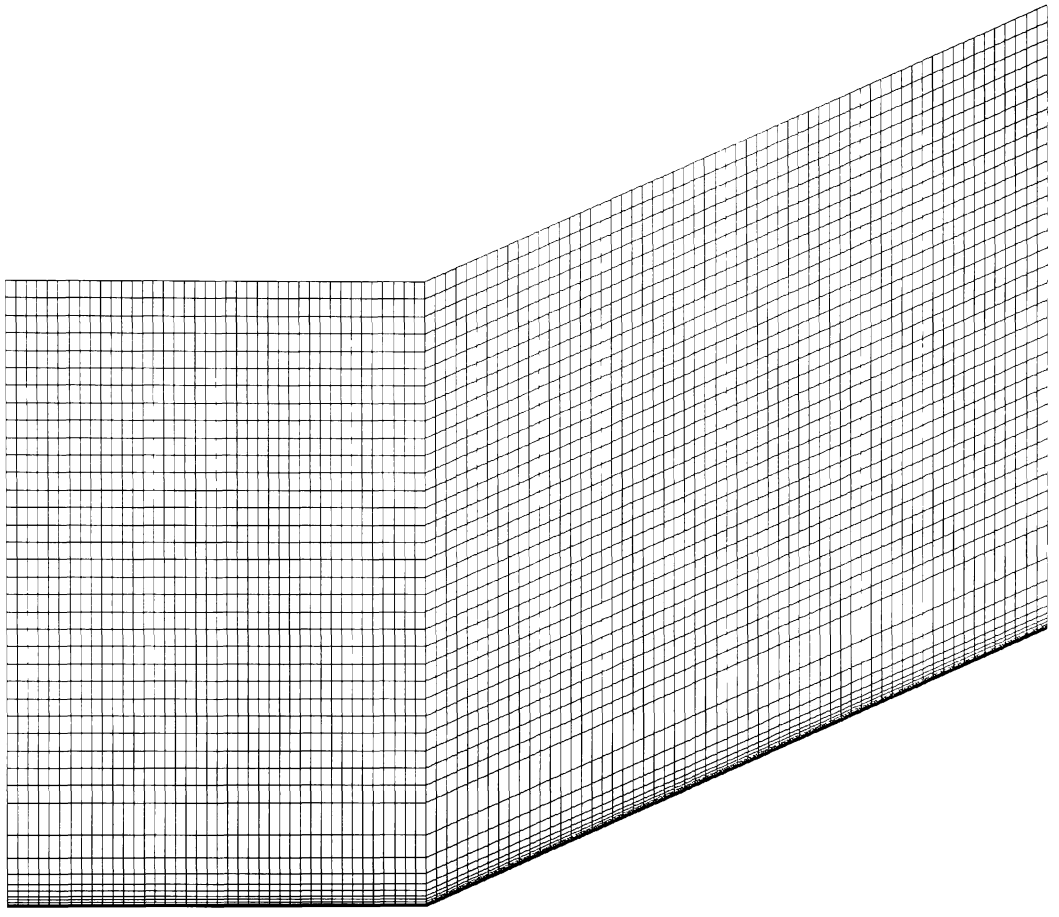

Figure 8: Computational Grid - Compression Corner

To ensure adequate grid resolution in the boundary layer, the y^+ value of the first grid point from the walls is approximately one.

To simulate air, a two-species mixture composed of 79% N_2 and 21% O_2 is used. The freestream conditions for the simulation are given in Table 2, where the values in brackets come directly from the experiment.

Freestream Conditions	
$T_\infty = 100$ K	($T_0 = 472$ °R)
$p_\infty = 23545$ Pa	($p_0 = 100$ psi)
$u_\infty = 571$ m/s	($M_\infty = 2.85$)
$k_\infty = 1E\text{-}8 * u_\infty^2 = 0.00326\ m^2/s^2$	
$\omega_\infty = 3870\ s^{-1}$	

Table 2: Freestream Conditions – Compression Corner

The turbulence intensity (1E-8), freestream specific dissipation rate, and surface-roughness height of 3.048 μm used for the wall boundary-condition of the specific dissipation rate, all come from the validation case of Wilcox. There is also an incoming boundary layer profile with defined values for all of the flow variables, also from Wilcox.

A similar experiment was conducted by Dolling and Murphy [29] at a Mach number of 2.90, and that data is included here as well for reference following the example of Wilcox. The results for the surface pressure are shown in Figure 9 where the compression corner location corresponds to x/h = 0, and h is the incoming boundary layer thickness. The results are compared to those of Wilcox who uses the MacCormack scheme with his 2006 version of the *k-ω* model, and Fluent using the Roe flux-difference splitting scheme with the Wilcox (1998) *k-ω* model.

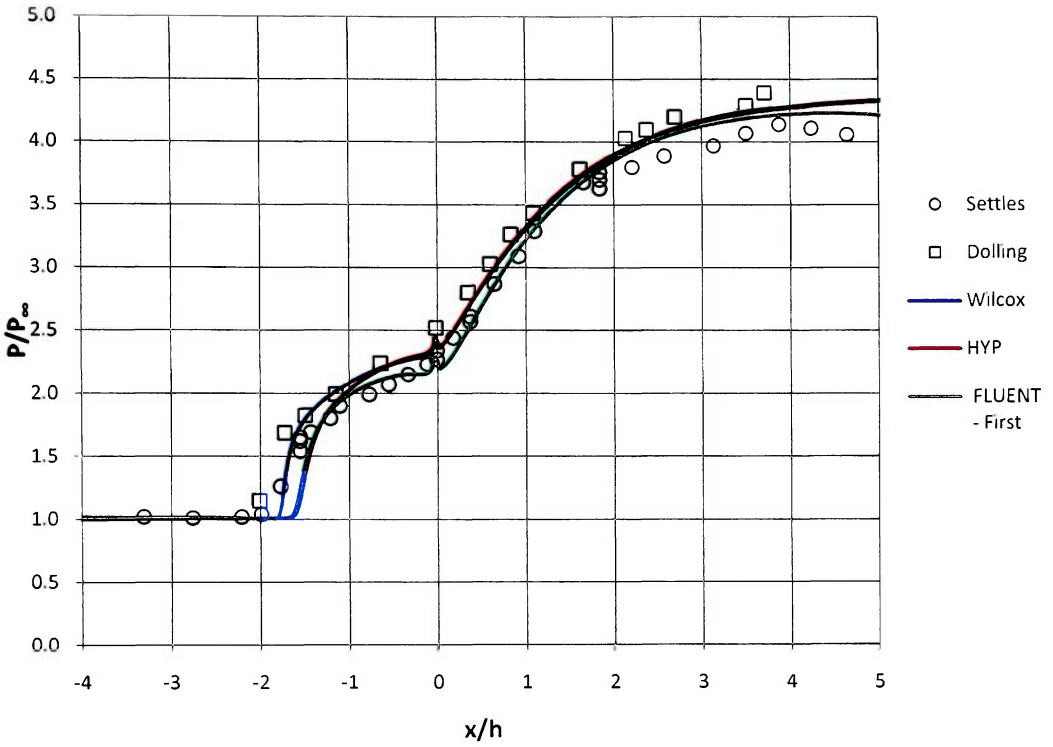

Figure 9: Surface Pressure – Compression Corner

The first-order solutions of HYP and Fluent predict flow separation further downstream than the actual separation point. Also note the Wilcox (1998) k-ω model used by Fluent does not include the stress limiter or cross diffusion, but it is unlikely that this is the cause of the differences seen here. A percent-error comparison of the solutions is shown in Figure 10.

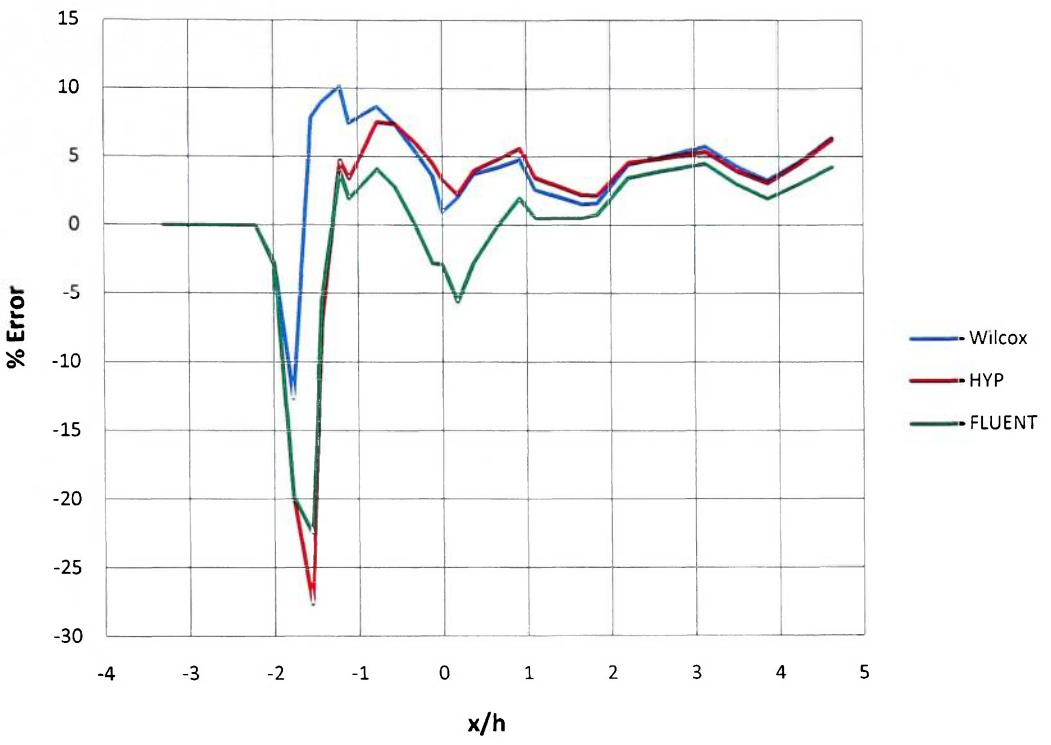

Figure 10: Percent Error - Compression Corner

It can be seen that Wilcox is more accurate at predicting separation, but shortly thereafter Fluent, for the most part, has the least amount of error. The RMS error for Wilcox, HYP, and Fluent is 5.63, 7.76, and 6.34 percent respectively.

In Figure 11, the pressure contours show where the flow separates upstream of the corner and then reattaches further up the ramp.

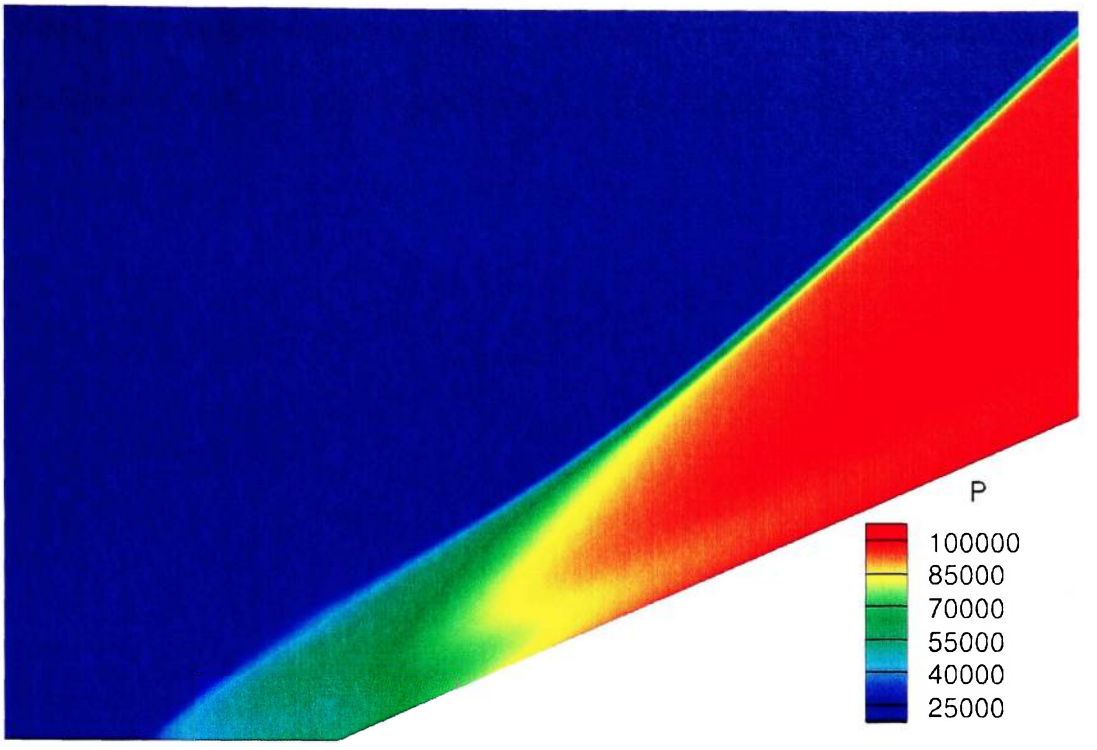

Figure 11: Pressure Contours – Compression Corner

The grid for this case has 80,000 cells which is significantly more than the backward-facing step case. As a result, the computation time is considerably longer. The explicit scheme used in HYP takes 10 days, whereas the MacCormack fully-implicit scheme used by Wilcox takes only 1 hour. To improve the performance of HYP, a grid sequencing method was also added to the code. This decreases the number of cells in the original grid, and then adds cells as the solution progresses until the original grid is again obtained. Using this method, the solution time is decreased from 10 days to 1 day.

As was seen in the previous validation case, the first-order results are not sufficiently accurate, and a second-order upwind scheme should be considered.

Also, it is now apparent that an implicit scheme will be beneficial, especially for practical applications where a large number of cells will be required.

Chapter 6

Summary

6.1 Overview of Results

A two-equation turbulence model for hypersonic flows has been extended to multiple species and implemented using Steger-Warming flux-vector splitting. In the derivation of the eigenvalues it was found that the presence of turbulence affects the speed of sound. The inviscid verification case was successful with less than 1% error when compared to the analytical results. For this verification, only scalar transport of the turbulence kinetic energy and specific dissipation rate was calculated: source terms were neglected. Two turbulent cases were used for validation: supersonic flow past a backward-facing step and into a compression corner. For the backward-facing step simulation, the surface pressure has a maximum error of 63% in the separation region, less than 5% error after the flow reattaches, and an RMS error of 17.2%. Compared to the results of Wind-US and Cobalt, HYP has the least error, both RMS and maximum. For the compression corner case, the surface pressure has a maximum error of 27% in the separation region, roughly 5% error downstream of separation, and an RMS error of 7.76%. In this case, HYP has the largest RMS and maximum error compared to Fluent and Wilcox.

6.2 Future Recommendations

The implementation of an implicit scheme should be the first task, so as to make all future simulations time-efficient. Secondly, the inviscid fluxes need to have second-order accuracy to improve the results. Also, due to the limited amount of verification performed, it would be beneficial to check that the law of the wall is observed in a turbulent boundary layer. After completing these initial tasks, the turbulence model can then be tested more rigorously: systematic validation for three-dimensional reacting flows, for which Wilcox has not validated this model. First, 3-D cases can be run to see if the closure coefficients require retuning, and then reactions can be added for final validation.

REFERENCES

1. Moin, P. and Mahesh, K., "Direct Numerical Simulation – A Tool in Turbulence Research," Annual Review of Fluid Mechanics, Vol. 30 (1998): 539-578.

2. Cebeci, T. and Smith, A. M. O., Analysis of Turbulent Boundary Layers, Ser. in Applied Mathematics and Mechanics. Vol. 15. Orlando: Academic Press, 1974.

3. Baldwin, B. S. and Lomax, H., "Thin-Layer Approximation and Algebraic Model for Separated Turbulent Flows," AIAA Paper 78-257, 1978.

4. Baldwin, B. S. and Barth, T. J., "A One-Equation Turbulence Transport Model for High Reynolds Number Wall-Bounded Flows," AIAA Paper 91-0610, 1991.

5. Spalart, P. R. and Allmaras, S. R., "A One-Equation Turbulence Model for Aerodynamic Flows," AIAA Paper 92-439, 1992.

6. Launder, B. E. and Sharma, B. I., "Application of the Energy Dissipation Model of Turbulence to the Calculation of Flow Near a Spinning Disk," Letters in Heat and Mass Transfer, Vol. 1, No. 2 (1974): 131-138.

7. Wilcox, D. C., Turbulence Modeling for CFD, 3rd ed. DCW Industries, Inc., 2006.

8. Menter, F. R., "Two-Equation Eddy-Viscosity Turbulence Models for Engineering Applications," AIAA Journal, Vol. 32, No. 8, August 1994: 1598-1605.

9. Sagaut, P. and Germano, M., Large Eddy Simulation for Incompressible Flows, 2nd ed. New York: Springer-Verlag, 2004.

10. Spalart, P. R., Jou, W.-H., Strelets, M. and Allmaras, S. R., "Comments on the Feasibility of LES for Wings, and on a Hybrid RANS/LES Approach," Advances in DNS/LES, (C. Liu and Z. Liu, eds. – Proceedings of 1st AFOSR International Conference on DNS and LES, Louisiana Tech.), Columbus, OH: Greyden Press, 1997.

11. Perrell, E. R., Erickson, W. D. and Candler, G. V., "Numerical Simulation of Nonequilibrium Condensation in a Hypersonic Wind Tunnel," Journal of Thermophysics and Heat Transfer, Vol. 10, No. 2, pp. 277-283, April-June 1996.

12. Moss, J. M. and Perrell, E. R., "CFD Analysis of Combined Cycle Scramjet/Rocket," AIAA 2005-4426, 41st AIAA/ASME Joint Propulsion Conference, Tucson, AZ, July 11-13, 2005.

13. Thomas, S., Britton, D., Perrell, E., Liron, C., Cassibry, J., Chiroux, R. and Adams, R., "Verification of a Multiphysics Toolkit against the Magnetized Target Fusion Concept," AIAA 2005-4141, 41st AIAA/ASME/SAE/ASEE Joint Propulsion Conference and Exhibit, Tucson, AZ, July 11-13, 2005.

14. Steger, J. L. and Warming, R. F., "Flux Vector Splitting of the Inviscid Gasdynamic Equations with Application to Finite-Difference Methods," NASA TM-78605, 1979.

15. Wey, T. C. and Li, C. P., "Comparison of Flux-Vector and Flux-Difference Splitting Techniques for Hypersonic Flow," AIAA Paper 88-3648, 1988.

16. Wilcox, D. C., "Comparison of Two-Equation Turbulence Models for Boundary Layers with Pressure Gradient," AIAA Journal, Vol. 31, No. 8, pp. 1414-1421, 1993.

17. Tennekes, H. and Lumley, J. L., A First Course in Turbulence, Cambridge: MIT Press, 1972.

18. Davidson, P. A., Turbulence: An Introduction for Scientists and Engineers, Oxford: Oxford University Press, 2004.

19. Schlichting, H. and Gersten, K., Boundary Layer Theory, 8th ed. New York: Springer, 2000.

20. Dash, S. M., Perrell, E. R., Kenzakowski, D. C., and Chidambaram, N., "Turbulent Effects on Missile Lateral Control/Divert Jet Interactions," AIAA 99-0809, 37th AIAA Aerospace Sciences Meeting and Exhibit, Reno, NV, January 11-14, 1999.

21. Schmitt, F. and Perrell, E., "The HYP CFD User's Manual," Ver. 1.0. Unpublished manual, 2006.

22. Hirsch, C., Numerical Computation of Internal and External Flows, Vol. 2. New York: Wiley, 1990.

23. Siikonen, T., "An Application of Roe's Flux-Difference Splitting for k-ε Turbulence Model," International Journal for Numerical Methods in Fluids, Vol. 21, Issue 11, pp. 1017-1039, 1995.

24. Anderson, J. D., Jr., Computational Fluid Dynamics: The Basics with Applications, New York: McGraw-Hill, 1995.

25. Tannehill, J. C., Anderson, D. A., and Pletcher, R. H., Computational Fluid Mechanics and Heat Transfer, 2nd ed. Philadelphia: Taylor & Francis, 1997.

26. Smith, H. E., "The Flow Field and Heat Transfer Downstream of a Rearward Facing Step in Supersonic Flow," ARL-67-0056, 1967.

27. Wilcox, D. C., Companion Software: Turbulence Modeling for CFD, 3rd ed. DCW Industries, Inc., 2006.

28. Settles, G. S., Vas, I. E., and Bogdonoff, S. M., "Details of a Shock Separated Turbulent Boundary Layer at a Compression Corner," AIAA Journal, Vol. 14, No. 12, pp. 1709-1715, 1976.

29. Dolling, D. S. and Murphy, M. T., "Unsteadiness of the Separation Shock Wave Structure in a Supersonic Compression Ramp Flowfield," AIAA Journal, Vol. 21, No. 12, pp. 1628-1634, 1983.

APPENDIX

$$
\frac{\partial \mathbf{V}}{\partial \mathbf{Q}} = \begin{bmatrix}
1 & 0 & 0 & 0 & 0 & 0 & 0 & 0 \\
0 & 1 & 0 & 0 & 0 & 0 & 0 & 0 \\
-\frac{\tilde{u}}{\bar{\rho}} & -\frac{\tilde{u}}{\bar{\rho}} & \frac{1}{\bar{\rho}} & 0 & 0 & 0 & 0 & 0 \\
-\frac{\tilde{v}}{\bar{\rho}} & -\frac{\tilde{v}}{\bar{\rho}} & 0 & \frac{1}{\bar{\rho}} & 0 & 0 & 0 & 0 \\
-\frac{\tilde{w}}{\bar{\rho}} & -\frac{\tilde{w}}{\bar{\rho}} & 0 & 0 & \frac{1}{\bar{\rho}} & 0 & 0 & 0 \\
\left(e_k - h_{f_1} - \tilde{h}_1\right)(\gamma - 1) + \gamma R_1 \tilde{T} & \left(e_k - h_{f_{ns}} - \tilde{h}_{ns}\right)(\gamma - 1) + \gamma R_{ns} \tilde{T} & -\tilde{u}(\gamma - 1) & -\tilde{v}(\gamma - 1) & -\tilde{w}(\gamma - 1) & \gamma - 1 & -(\gamma - 1) & 0 \\
-\frac{k}{\bar{\rho}} & -\frac{k}{\bar{\rho}} & 0 & 0 & 0 & 0 & \frac{1}{\bar{\rho}} & 0 \\
-\frac{\omega}{\bar{\rho}} & -\frac{\omega}{\bar{\rho}} & 0 & 0 & 0 & 0 & 0 & \frac{1}{\bar{\rho}}
\end{bmatrix}
$$

$$
\frac{\partial \mathbf{F}'}{\partial \mathbf{V}} = \begin{bmatrix}
\tilde{u}' & 0 & \xi_x \bar{\rho}_1 & \xi_y \bar{\rho}_1 & \xi_z \rho_1 & 0 & 0 & 0 \\
0 & \tilde{u}' & \xi_x \rho_{ns} & \xi_y \bar{\rho}_{ns} & \xi_z \bar{\rho}_{ns} & 0 & 0 & 0 \\
\tilde{u}'\tilde{u} + \xi_x \frac{2}{3} k & \tilde{u}'\tilde{u} + \xi_x \frac{2}{3} k & \bar{\rho}\tilde{u}' + \xi_x \rho \tilde{u} & \xi_y \bar{\rho}\tilde{u} & \xi_z \bar{\rho}\tilde{u} & \xi_x & \xi_x \frac{2}{3}\rho & 0 \\
\tilde{u}'\tilde{v} + \xi_y \frac{2}{3} k & \tilde{u}'\tilde{v} + \xi_y \frac{2}{3} k & \xi_x \bar{\rho}\tilde{v} & \bar{\rho}\tilde{u}' + \xi_y \bar{\rho}\tilde{v} & \xi_z \bar{\rho}\tilde{v} & \xi_y & \xi_y \frac{2}{3}\rho & 0 \\
\tilde{u}'\tilde{w} + \xi_z \frac{2}{3} k & \tilde{u}'\tilde{w} + \xi_z \frac{2}{3} k & \xi_x \bar{\rho}\tilde{w} & \xi_y \bar{\rho}\tilde{w} & \rho\tilde{u}' + \xi_z \bar{\rho}\tilde{w} & \xi_z & \xi_z \frac{2}{3}\bar{\rho} & 0 \\
\tilde{u}'\left(h_{f_1} + \tilde{h}_1 - \frac{\gamma R_1 \tilde{T}}{\gamma - 1} + e_k + \frac{5}{3}k\right) & \tilde{u}'\left(h_{f_{ns}} + \tilde{h}_{ns} - \frac{\gamma R_{ns} T}{\gamma - 1} + e_k + \frac{5}{3}k\right) & \bar{\rho}\tilde{u}'\tilde{u} + \xi_x \bar{\rho}\left(h_f + \tilde{h} + e_k + \frac{5}{3}k\right) & \bar{\rho}\tilde{u}'\tilde{v} + \xi_y \bar{\rho}\left(h_f + \tilde{h} + e_k + \frac{5}{3}k\right) & \bar{\rho}\tilde{u}'\tilde{w} + \xi_z \bar{\rho}\left(h_f + \tilde{h} + e_k + \frac{5}{3}k\right) & \frac{\tilde{u}'\gamma}{\gamma - 1} & \frac{5}{3}\bar{\rho}\tilde{u}' & 0 \\
\tilde{u}'k & \tilde{u}'k & \xi_x \bar{\rho}k & \xi_y \bar{\rho}k & \xi_z \bar{\rho}k & 0 & \bar{\rho}\tilde{u}' & 0 \\
\tilde{u}'\omega & \tilde{u}'\omega & \xi_x \bar{\rho}\omega & \xi_y \bar{\rho}\omega & \xi_z \bar{\rho}\omega & 0 & 0 & \bar{\rho}\tilde{u}'
\end{bmatrix}
$$

$$\tilde{\mathbf{R}} = \begin{bmatrix} 1 & \cdots & 0 & 0 & 0 & 0 & 0 & \bar{\rho}_1 & \bar{\rho}_1 \\ \vdots & \ddots & \vdots & \vdots & \vdots & \vdots & \vdots & \vdots & \vdots \\ 0 & \cdots & 1 & 0 & 0 & 0 & 0 & \bar{\rho}_{ns} & \bar{\rho}_{ns} \\ 0 & \cdots & 0 & -\xi_y & -\xi_z & 0 & 0 & \xi_x a_k & -\xi_x a_k \\ 0 & \cdots & 0 & \xi_x & 0 & 0 & 0 & \xi_y a_k & -\xi_y a_k \\ 0 & \cdots & 0 & 0 & \xi_x & 0 & 0 & \xi_z a_k & -\xi_z a_k \\ -\frac{2}{3}k & \cdots & -\frac{2}{3}k & 0 & 0 & -\frac{2}{3}\bar{\rho} & 0 & \bar{\rho}\left(a_k^2 - \frac{2}{3}k\right) & \bar{\rho}\left(a_k^2 - \frac{2}{3}k\right) \\ 0 & \cdots & 0 & 0 & 0 & 1 & 0 & 0 & 0 \\ 0 & \cdots & 0 & 0 & 0 & 0 & 1 & 0 & 0 \end{bmatrix}$$

$$\tilde{\mathbf{L}} = \begin{bmatrix} 1 - \frac{2\bar{\rho}_1 k}{3\bar{\rho}a_k^2} & \cdots & -\frac{2\bar{\rho}_1 k}{3\bar{\rho}a_k^2} & 0 & 0 & 0 & -\frac{\bar{\rho}_1}{\bar{\rho}a_k^2} & -\frac{2\bar{\rho}_1}{3a_k^2} & 0 \\ \vdots & \ddots & \vdots & \vdots & \vdots & \vdots & \vdots & \vdots & \vdots \\ -\frac{2\bar{\rho}_{ns} k}{3\bar{\rho}a_k^2} & \cdots & 1 - \frac{2\bar{\rho}_{ns} k}{3\bar{\rho}a_k^2} & 0 & 0 & 0 & -\frac{\bar{\rho}_{ns}}{\bar{\rho}a_k^2} & -\frac{2\bar{\rho}_{ns}}{3a_k^2} & 0 \\ 0 & \cdots & 0 & -\xi_y & \frac{\xi_x^2+\xi_z^2}{\xi_x} & -\frac{\xi_y\xi_z}{\xi_x} & 0 & 0 & 0 \\ 0 & \cdots & 0 & -\xi_z & -\frac{\xi_y\xi_z}{\xi_x} & \frac{\xi_x^2+\xi_y^2}{\xi_x} & 0 & 0 & 0 \\ 0 & \cdots & 0 & 0 & 0 & 0 & 0 & 1 & 0 \\ 0 & \cdots & 0 & 0 & 0 & 0 & 0 & 0 & 1 \\ \frac{k}{3\bar{\rho}a_k^2} & \cdots & \frac{k}{3\bar{\rho}a_k^2} & \frac{\xi_x}{2a_k} & \frac{\xi_y}{2a_k} & \frac{\xi_z}{2a_k} & \frac{1}{2\bar{\rho}a_k^2} & \frac{1}{3a_k^2} & 0 \\ \frac{k}{3\bar{\rho}a_k^2} & \cdots & \frac{k}{3\bar{\rho}a_k^2} & -\frac{\xi_x}{2a_k} & -\frac{\xi_y}{2a_k} & -\frac{\xi_z}{2a_k} & \frac{1}{2\bar{\rho}a_k^2} & \frac{1}{3a_k^2} & 0 \end{bmatrix}$$

$$
\mathbf{R} = \begin{bmatrix}
1 & \cdots & 0 & 0 & 0 & 0 & 0 & \bar{\rho}_1 & \bar{\rho}_1 \\
\vdots & \ddots & \vdots & \vdots & \vdots & \vdots & \vdots & \vdots & \vdots \\
0 & \cdots & 1 & 0 & 0 & 0 & 0 & \bar{\rho}_{ns} & \bar{\rho}_{ns} \\
\tilde{u} & \cdots & \tilde{u} & -\xi_y\bar{\rho} & -\xi_z\bar{\rho} & 0 & 0 & \bar{\rho}[\tilde{u}+\xi_x a_k] & \bar{\rho}[\tilde{u}-\xi_x a_k] \\
\tilde{v} & \cdots & \tilde{v} & \xi_x\bar{\rho} & 0 & 0 & 0 & \bar{\rho}[\tilde{v}+\xi_y a_k] & \bar{\rho}[\tilde{v}-\xi_y a_k] \\
\tilde{w} & \cdots & \tilde{w} & 0 & \xi_x\bar{\rho} & 0 & 0 & \bar{\rho}[\tilde{w}+\xi_z a_k] & \bar{\rho}[\tilde{w}-\xi_z a_k] \\
\psi + h_{f_1} + \tilde{h}_1 - \frac{\gamma R_1 \tilde{T}}{\gamma-1} & \cdots & \psi + h_{f_{ns}} + \tilde{h}_{ns} - \frac{\gamma R_{ns}\tilde{T}}{\gamma-1} & \bar{\rho}(\xi_x\tilde{v}-\xi_y\tilde{u}) & \bar{\rho}(\xi_x\tilde{w}-\xi_z\tilde{u}) & \frac{\bar{\rho}\left(\gamma-\frac{5}{3}\right)}{\gamma-1} & 0 & \phi + \bar{\rho}\tilde{u}' a_k & \phi - \bar{\rho}\tilde{u}' a_k \\
k & \cdots & k & 0 & 0 & \bar{\rho} & 0 & \bar{\rho}k & \bar{\rho}k \\
\omega & \cdots & \omega & 0 & 0 & 0 & \bar{\rho} & \bar{\rho}\omega & \bar{\rho}\omega
\end{bmatrix}
$$

$$
\mathbf{L} = \begin{bmatrix}
1 - \frac{\bar{\rho}_1\left[\left(e_k - h_{f_1} - \tilde{h}_1\right)(\gamma-1) + \gamma R_1 \tilde{T}\right]}{\bar{\rho}a_k^2} & \cdots & -\frac{\bar{\rho}_1\left[\left(e_k - h_{f_{ns}} - \tilde{h}_{ns}\right)(\gamma-1) + \gamma R_{ns} \tilde{T}\right]}{\bar{\rho}a_k^2} & \frac{\bar{\rho}_1\tilde{u}(\gamma-1)}{\bar{\rho}a_k^2} & \frac{\bar{\rho}_1\tilde{v}(\gamma-1)}{\bar{\rho}a_k^2} & \frac{\bar{\rho}_1\tilde{w}(\gamma-1)}{\bar{\rho}a_k^2} & -\frac{\bar{\rho}_1(\gamma-1)}{\bar{\rho}a_k^2} & \frac{\bar{\rho}_1\left(\gamma-\frac{5}{3}\right)}{\bar{\rho}a_k^2} & 0 \\
\vdots & \cdot & \vdots & \vdots & \vdots & \vdots & \vdots & \vdots & \vdots \\
-\frac{\bar{\rho}_{ns}\left[\left(e_k - h_{f_1} - \tilde{h}_1\right)(\gamma-1) + \gamma R_1 \tilde{T}\right]}{\bar{\rho}a_k^2} & \cdots & 1 - \frac{\bar{\rho}_{ns}\left[\left(e_k - h_{f_{ns}} - \tilde{h}_{ns}\right)(\gamma-1) + \gamma R_{ns} \tilde{T}\right]}{\bar{\rho}a_k^2} & \frac{\bar{\rho}_{ns}\tilde{u}(\gamma-1)}{\bar{\rho}a_k^2} & \frac{\bar{\rho}_{ns}\tilde{v}(\gamma-1)}{\bar{\rho}a_k^2} & \frac{\bar{\rho}_{ns}\tilde{w}(\gamma-1)}{\bar{\rho}a_k^2} & -\frac{\bar{\rho}_{ns}(\gamma-1)}{\bar{\rho}a_k^2} & \frac{\bar{\rho}_{ns}\left(\gamma-\frac{5}{3}\right)}{\bar{\rho}a_k^2} & 0 \\
\frac{\xi_y\tilde{u}' - \tilde{v}}{\xi_x\bar{\rho}} & \cdots & \frac{\xi_y\tilde{u}' - \tilde{v}}{\xi_x\bar{\rho}} & -\frac{\xi_y}{\bar{\rho}} & \frac{\xi_x^2+\xi_z^2}{\xi_x\bar{\rho}} & -\frac{\xi_y\xi_z}{\xi_x\bar{\rho}} & 0 & 0 & 0 \\
\frac{\xi_z\tilde{u}' - \tilde{w}}{\xi_x\bar{\rho}} & \cdots & \frac{\xi_z\tilde{u}' - \tilde{w}}{\xi_x\bar{\rho}} & -\frac{\xi_z}{\bar{\rho}} & -\frac{\xi_y\xi_z}{\xi_x\bar{\rho}} & \frac{\xi_x^2+\xi_y^2}{\xi_x\bar{\rho}} & 0 & 0 & 0 \\
-\frac{k}{\bar{\rho}} & \cdots & -\frac{k}{\bar{\rho}} & 0 & 0 & 0 & 0 & \frac{1}{\bar{\rho}} & 0 \\
-\frac{\omega}{\bar{\rho}} & \cdots & -\frac{\omega}{\bar{\rho}} & 0 & 0 & 0 & 0 & 0 & \frac{1}{\bar{\rho}} \\
\frac{\left(e_k - h_{f_1} - \tilde{h}_1\right)(\gamma-1) + \gamma R_1 \tilde{T} - \tilde{u}' a_k}{2\bar{\rho}a_k^2} & \cdots & \frac{\left(e_k - h_{f_{ns}} - \tilde{h}_{ns}\right)(\gamma-1) + \gamma R_{ns} \tilde{T} - \tilde{u}' a_k}{2\bar{\rho}a_k^2} & \frac{\xi_x a_k - \tilde{u}(\gamma-1)}{2\bar{\rho}a_k^2} & \frac{\xi_y a_k - \tilde{v}(\gamma-1)}{2\bar{\rho}a_k^2} & \frac{\xi_z a_k - \tilde{w}(\gamma-1)}{2\bar{\rho}a_k^2} & \frac{\gamma-1}{2\bar{\rho}a_k^2} & -\frac{\gamma-\frac{5}{3}}{2\bar{\rho}a_k^2} & 0 \\
\frac{\left(e_k - h_{f_1} - \tilde{h}_1\right)(\gamma-1) + \gamma R_1 \tilde{T} + \tilde{u}' a_k}{2\bar{\rho}a_k^2} & \cdots & \frac{\left(e_k - h_{f_{ns}} - \tilde{h}_{ns}\right)(\gamma-1) + \gamma R_{ns} \tilde{T} + \tilde{u}' a_k}{2\bar{\rho}a_k^2} & \frac{-\xi_x a_k - \tilde{u}(\gamma-1)}{2\bar{\rho}a_k^2} & \frac{-\xi_y a_k - \tilde{v}(\gamma-1)}{2\bar{\rho}a_k^2} & \frac{-\xi_z a_k - \tilde{w}(\gamma-1)}{2\bar{\rho}a_k^2} & \frac{\gamma-1}{2\bar{\rho}a_k^2} & -\frac{\gamma-\frac{5}{3}}{2\bar{\rho}a_k^2} & 0
\end{bmatrix}
$$

$$
\psi = e_k + \frac{k\left(\gamma-\frac{5}{3}\right)}{\gamma-1} \qquad \phi = \bar{\rho}E + P + \frac{2}{3}\bar{\rho}k
$$